nature chemistry

SUPPLEMENTARY INFORMATION

DOI: 10.1038/NCHEM.2544

High-resolution mapping of bifurcations in nonlinear biochemical circuits

A.J. Genot, A. Baccouche, R. Sieskind, N. Aubert-Kato,
N. Bredeche, J.F. Bartolo, V. Taly, T. Fujii, Y. Rondelez

Contents

S1 Materials and methods

S1.1 Sequences and strand design

DNA strands were ordered from Biomers (Germany). The sequences are indicated in Table 1. For fluorescent reporting, we use nucleobase quenching [1] to report on the levels of α and β in the bistable switch. It uses the fact the fluorescence of a dye attached to the 3' or 5' end of a ssDNA shifts up or down when this strand becomes double-stranded. We attach a TAMRA dye (positive shift upon binding of β) to the template βtoiα and a FAM dye (negative shift upon binding of α) to the template αtoiβ. It must be kept in mind that fluorescence shifts do not vary linearly with the concentration of free triggers, although their relation is expected to be monotonic. For the predator-prey network, we use a dual-labelled template, and note that the fluorescence level of TAMRA (our observable) shifts positively upon hybridization of prey strands.

		Sequence 5' -> 3'	3' modification	5' modification
Bistable switch	αtoα	C*C*A*AGACUCAGCCAAGACTCAG	Phosphate	
	βtoβ	A*A*C*AGACUCGAAACAGACTCGA	Phosphate	
	βtoiα	T*T*A*CTCAGCCAAGACAACAGACTCGA	TAMRA	
	αtoiβ	T*T*A*CTCGAAACAGACCCAAGACTCAG	FAM	
	α	CTGAGTCTTGG		
	β	TCGAGTCTGTT		
Predator-prey	Grass Template	C*G*G*C*C*GAATGCGGCCGAATG	TAMRA	JOE
	Prey	CATTCGGCCG		
	Predator	CATTCGGCCGAATG		

Table 1: Sequences of DNA strands used in the bistable switch and predator prey networks. Stars correspond to a phosphorothioate modification (which prevents degradation from the exonuclease).

For generating the diagram of the bistable switch, the master mix contains the following reagents : Tris-HCl (45 mM, pH-8.4), NaCl (50 mM), KCl (10 mM), Mg^{2+} (from $MgCl_2$ + $MgSO_4$, 7 mM in total), $(NH_4)_2SO_4$ (10 mM), dNTPs (400 µM each, New England Biolabs, NEB), Synperonic F108 (0,1% v/w, Sigma-Aldrich), Netropsin (2 µM, Sigma-Aldrich), Dithiothreitol (3.5 mM, Sigma-Aldrich), BSA (500 $\mu g.mL^{-1}$, NEB); the enzymes: polymerase Bst 2.0 WarmStart™ (4 $units.mL^{-1}$, NEB), exonuclease ttRecJ (20 nM), and nickase Nt.BstNBI (100 $units.mL^{-1}$, NEB), the inhibitor-producer templates (βtoiα and αtoiβ, 20 nM each). We use a Warmstart version of the polymerase to mitigate production delays associated with the microfluidic protocol. The above buffer was assembled by mixing a ThermoPol DF reaction buffer at 1X (NEB) and a NEB 3 buffer at 0.5X (NEB), and completing with the specified additional components.

This mix is then split into two sets of 3 tubes and completed with parametric species and their fluorescent barcodes (we show in S6 that the barcodes have no effect on the reactivity):

- [αtoα] = 500 nM, [βtoβ] = 0 nM barcoded with 200 nM of Dextran Alexa Fluor 647 (10,000 MW, Life Technologies)
- [αtoα] = 0 nM, [βtoβ] = 500 nM barcoded with 200 nM of Dextran Cascade Blue (10,000 MW, Life Technologies)
- [αtoα] = 0 nM, [βtoβ] = 0 nM, 5 nM of Dextran Cascade Blue, 20 nM of Dextran Alexa Fluor 647 (this base level of Dextran raises their minimal fluorescence over the limit of detection of the microscope and thus improves quantification for low concentrations of template) and water for volume compensation.

The sets differ by their [α]/[β] ratio, corresponding to an initial state αβ=01 (0.1 nM of α and 10.1 nM of β) or αβ=10 (10.1 nM of α and 0.1 nM of β). For the independent 1D scans we use only two tubes ([βtoβ] = 0 or 500 nM).

Predator-Prey: we prepare a master mix containing 20 mM Tris-HCl, 10 mM $(NH_4)_2SO_4$, 10 mM KCl, 50 mM NaCl, 8 mM $MgSO_4$, 0.1 % Synperonic F108, dNTPs (400 µM each), 2 µM Netropsin, 3 mM DTT, 500 µg/ml BSA, 400 $units.mL^{-1}$ Nb.BsmI (NEB) and 5 $\mu g.mL^{-1}$ of ETSSB (NEB). The prey strand is initially present at 20 nM, the predator strand at 10 nM. The master mix is split in 4 tubes and corresponding reagents are added:

- Template: 1.2 μM of template, and 200 nM Dextran Fluorescein (40,000 MW, Anionic, Lysine Fixable, Life Technologies)
- Polymerase: 9 % (v/v) of Bst 2.0 WarmStart DNA Polymerase (NEB, stock solution prediluted at 800 units.mL^{-1}) with 200 nM of Dextran Alexa Fluor 647
- Exonuclease: 18 % (v/v) of ttRecJ exonuclease (stock solution at 1.53 μM) with 200 nM of Dextran Cascade Blue
- Buffer compensation: with 20 nM of Alexa Fluor 647, 5 nM of Dextran Cascade Blue and 20 nM of Dextran FITC.

For droplet encapsulation, the surfactant was prepared from a perfluoropolyether carboxy-terminated polymer (Krytox, DuPont) and a polyetheramine (Jeffamine M1000, Huntsmann) based on the synthesis scheme described in [2]. The continuous phase is a mix of HFE 7500 oil (3M) with 2% (w/w) of surfactant.

S1.2 Microfluidic chip

The chip is shown in Fig. S1. The chips were made of PDMS and fabricated by standard soft lithography [3]. The mold was fabricated from a chrome mask. The height of the mold (SU-8 2050, MicroChem, USA) is measured optically to be 55 μm (+/- 10 μm). The chips were cured at 75^{o}C for 90 minutes, after which they were peeled off, plasma activated and bonded to glass slides. The chips were then baked for 5 hours at 200 ^{o}C to recover their hydrophobicity and improve bonding [4]. The chip comprises filters, resistances, one oil channel and 4 symmetric aqueous channels. The spacing of the filters was chosen to match that of the constriction (12.5 μm). We inserted resistances in the oil and aqueous channels (prior to the flow-focusing junction) in order to mitigate invasion from other channels and place the working pressure in the range accessible by our controller (see below). After the constriction, we added a serpentine channel for accelerating the internal mixing of the droplets and stabilizing the surfactant layer at the interface [5]. The pre-injector channel upstream of the junction is 300 μm long. Its length was chosen long enough to visualize the co-flow of aqueous channels, and short enough to minimize their contact time. Droplets are collected from the outlet in a pipette tip.

S1.2.1 Design of resistances

Microfluidic chips can be actuated by two means: flow control or pressure control. In our experiments, we need to rapidly scan a large number of combinations of concentrations, and thus we need a quick actuation. We chose pressure control because it is noticeably faster and more responsive. In an incompressible fluid, pressure jumps propagate instantly throughout the chip - allowing us to quickly modulate pressures near the junction by varying the pressures applied on the inlets. Indeed, for incompressible fluids ($div(v) = 0$) the pressure field satisfies an equation which does not contain any time-derivative: the pressure Poisson equation. In the laminar regime of microfluidics this equation reduces to the Laplace equation $\triangle P = 0$. The pressure is then an harmonic function whose value inside the chip is entirely determined by the chip's boundaries and the pressure applied on inlets and outlets. By contrast, jumps in flow rate do not propagate immediately -even in incompressible fluids - when channels are not rigid (which is known to be the case for PDMS and can be worsened by the elastic behaviour of tubing or connections [6]). Elastic channels act as fluidic capacitors that absorb jumps in flow rates and drastically slow down response times. But while pressure control allows for fast actuation, flow rates can become negative (back-flows). Cares need to be taken when programming the pressure profile to ensure that the content of a channel does not invade significantly another (slight invasion of a channel is still needed to ensure that the corresponding species' concentration sometime reaches 0 nM).

For sake of generality, we consider N aqueous channels (in our chip $N = 4$). All pressures are defined with respect to the atmospheric pressure P_o (pressure at the outlet). We neglect for this model the resistance of the pre-injector, which is short. Let P_i be the pressure of the aqueous inlet i, Q_i its flow rate and R its hydrodynamic resistance (identical for all aqueous channels). Similarly we define P_{oil}, Q_{oil} and R_{oil} the pressure, *total* flow rate and *equivalent* resistance of the two oil channels. Let P_{junc} be the pressure at the junction, Q_{out} the flow rate downstream of the junction and R_{out} the corresponding resistance. The pressure of the aqueous channel P_i and oil channel P_{out} are specified by the user through the pressure controller. On the other hand the flow rates (Q_i, Q_{out} and Q_{oil}) and the junction pressure P_{junc} are unknown variables. Those quantities are related linearly by

$$Q_i = (P_i - P_{junc})/R$$

$$Q_{oil} = (P_{oil} - P_{junc})/R_{oil}$$

$$Q_{out} = (P_{junc})/R_{out}$$

(Note that the viscosities of our HFE oil and water are similar). In order to avoid channel invasion, the flow rates Q_i must remain positive and thus $P_i \geqq P_{junc}$ (similar conditions also hold for the oil channels). We now investigate the constrains these equations place on the chip. From the conservation of volume for an incompressible flow, we have

$$Q_{out} = \sum_i Q_i + Q_{oil}$$

and thus

$$\frac{(P_{junc})}{R_{out}} = \frac{1}{R}\sum_i (P_i - P_{junc}) + \frac{P_{oil} - P_{junc}}{R_{oil}}$$

we can extract the junction pressure

$$P_{junc} = \frac{\sum_i P_i + P_{oil}\frac{R}{R_{oil}}}{\frac{R}{R_{out}} + N + \frac{R}{R_{oil}}}$$

Note that since the sum of aqueous pressures $\sum_i P_i$ and the oil pressure P_{oil} are kept constant, P_{junc} also remains constants during droplet generation.

Let us first consider the regime $R << R_{out,}R_{oil}$. The junction pressure is then simply the average of the pressures of aqueous inlet

$$P_{junc=}\frac{1}{N}\sum_i P_i$$

Since it is impossible for all the aqueous pressures to exceed their mean, at least one of the aqueous channel must be invaded. To avoid this, and provide a reasonable range of available pressures for the scanning process, we dimensionalized the resistances of the oil channels R_{oil} and the aqueous channels R to be noticeably larger than the resistance of the chip after the junction R_{out} (in the current design, $R_{oil} \simeq R$ and $R \simeq 80R_{out}$).

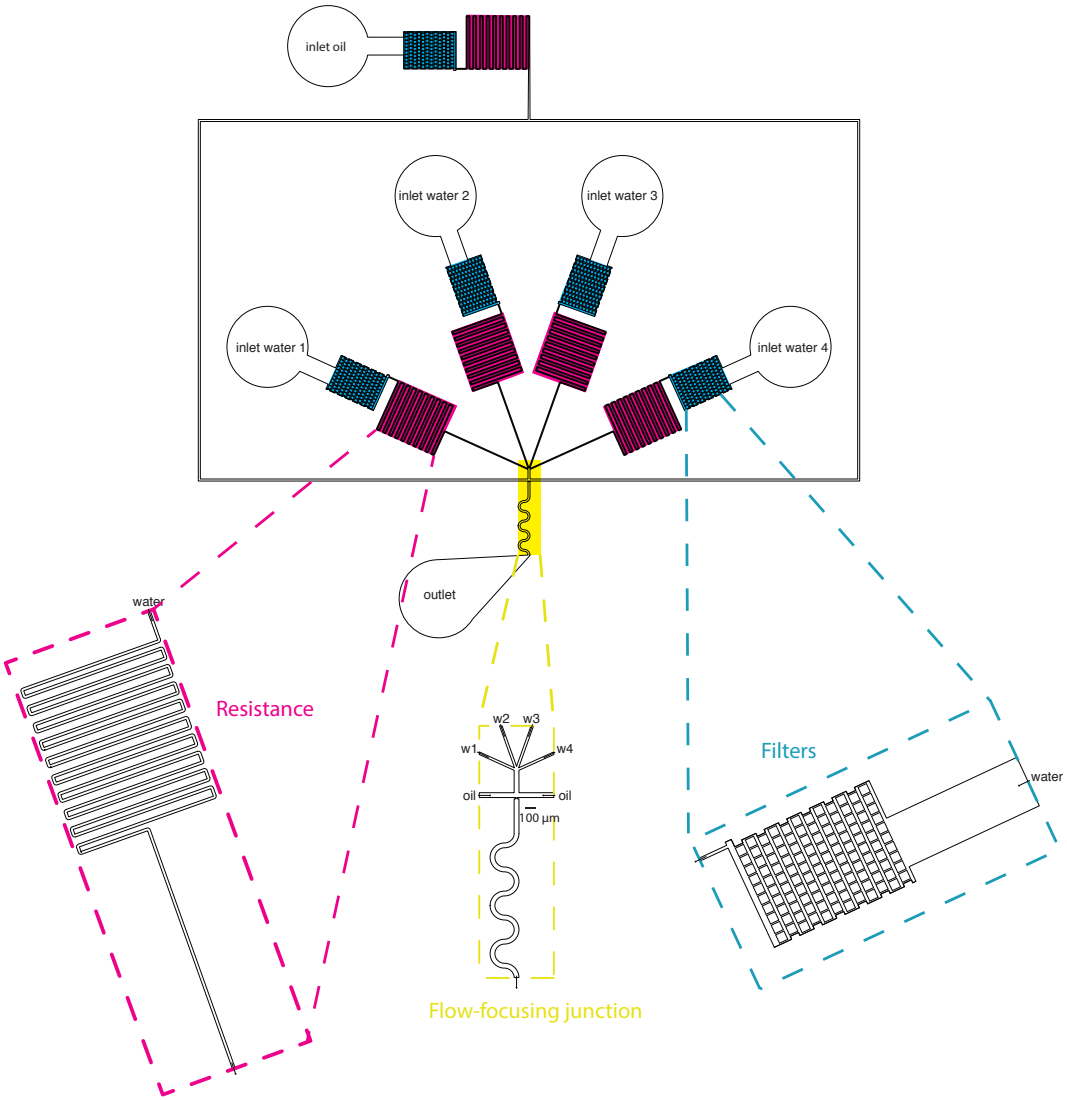

Figure S1: Microfluidic chip used for droplet generation. The chip comprises 4 aqueous inlets, one oil inlet and one collection outlet (the .dxf file is included as supplementary material). The width of the channel after the junction is 50 µm.

S1.2.2 Chip actuation

The chip was actuated with a pressure controller MFCS-EZ from Fluigent (France) (which claims a pressure resolution of ∼300 µbar, a setting time of ∼100 ms and a pressure stability <0.1% CV). The controller was pressurized by a nitrogen gas line (∼1000 mbar) and programmed through the scripting language AutoIt. PCR tubes (Bio-Bik T-02RTC) containing the reaction mixes sat at the bottom of 2mL tubes (Bio-Bik T334-6). Those reservoirs were connected to the chip through ∼30 cm of PEEK tubes (1/16 inch OD, 250 µm ID) which were directly inserted in the PDMS inlets. New PEEK tubes were freshly cut before each experiment to avoid cross contamination. The aqueous PCR tubes contained ∼50-100 µL of mix. Droplet generation was monitored with an epifluorescence microscope (Olympus IX71), illuminated with a LED system (Cool LED Pe) and controlled by MicroManager [7].

The pressures profiles were programmed as follows (Fig. S2). Note that the concentrations of species injected by a channel into the droplets is an affine function of the channel pressure -function which is identical for all aqueous channels by symmetry. Before launching the script, we assess the quality of chip fabrication by measuring for each

aqueous channel its minimum pressure P_{min} (the channel is invaded by other channels) and maximum pressure P_{max} (the channel fills the pre-injector and invades other channels) while keeping the total aqueous pressure constant. If the fabrication went well, P_{min} and P_{max} are similar for all channels. When that is not the case, we discard the chip. We also add routines for fluorescence calibration which follow the axes αtoα= 0nM or βtoβ= 0nM. The droplets in the apex of each arms contains 100% of the aqueous mixture of a given channel (Fig. S16). The script for each program has been added as Supplementary Information.

2D deterministic exploration (bistable switch, Fig. S2a): The pressure P_1 of channel 1 (containing say template αtoα) is quickly cycled from P_{min} to $P_{min} + (P_{max} - P_{min})/2$ in 20 constant steps. Meanwhile, the pressure P_2 of the channel 2 (containing the other template βtoβ) is slowly decremented from $P_{min} + (P_{max} - P_{min})/2$ to P_{min}. The pressure P_3 of the compensation channel is adjusted to keep the total aqueous pressure $P_1 + P_2 + P_3$ constant at 600 mbar. The cycle is then repeated, swapping the slow and fast pressures to symmetrize the exploration. The oil pressure is constant and set to 600 mbar. We repeat the whole process until ∼30 µL of emulsion is produced (∼25 minutes). For 1D scanning, there are only two channels and the pressure of each was simply scanned between P_{min} and P_{max} while keeping their sum constant.

3D Monte Carlo sampling (predator-prey oscillator, Fig. S2d): While a deterministic exploration is appropriate for a 2D space, it becomes prohibitively slow to run and complicated to code in a 3D space. Inspired by statistical methods for high-dimensional sampling, we turned to a "Monte-Carlo sampling" to explore the 3D parameter space of the predator prey. We generate with Mathematica a random walk in the $[0, 1]^3$ cube which we rescaled (in the scripting software) into $[P_{min}, P_{max}]^3$ after measuring P_{min} and P_{max}. We built the random walk by summing thousands of 3D increments $(\triangle_1, \triangle_2, \triangle_3)$, where each $\triangle_i$ is drawn independently from a Pareto distribution (typically with a power of ∼0.2 and a minimal value of ∼0.05). Pareto distributions have a long tail which ensures that the pressures sometimes "jump" abruptly to new regions of the cube - which is meant to improve coverage. We also apply reflections to the random walk so that it remains confined to the cube. The oil pressure is set to 700 mbar.

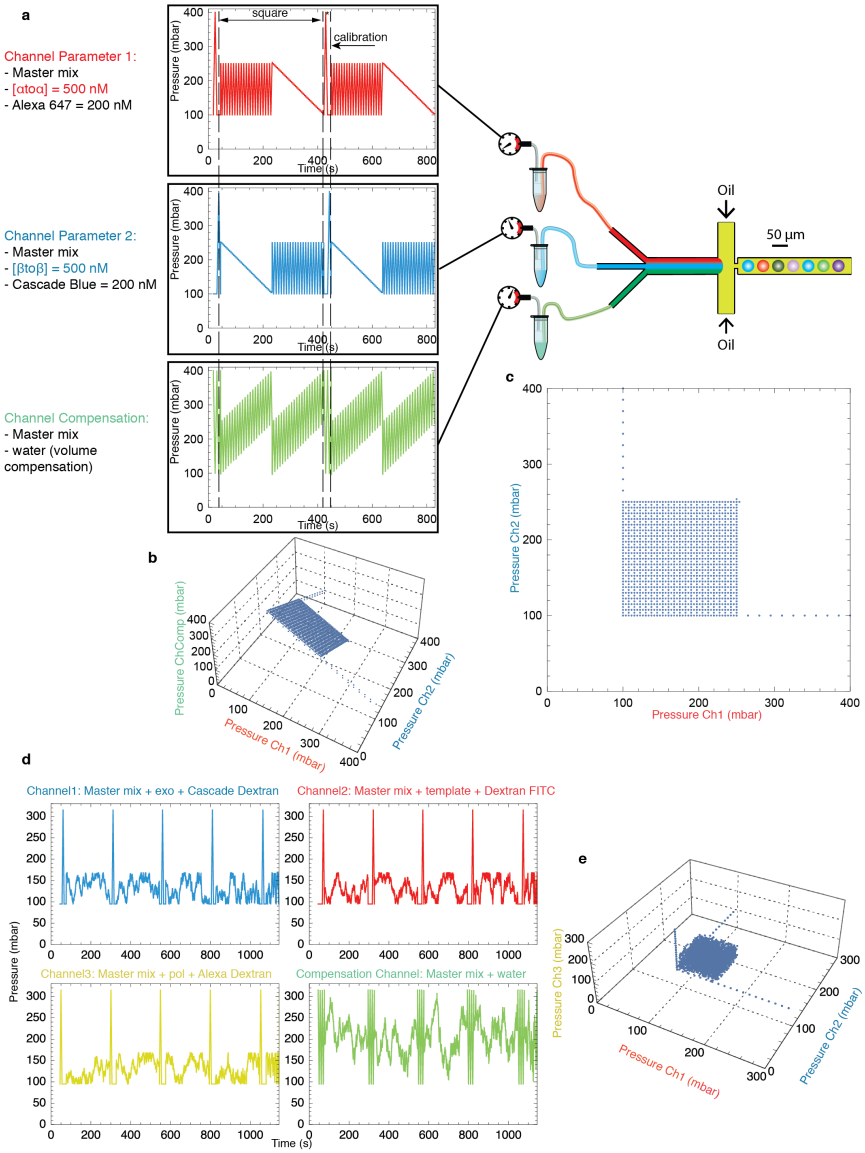

Figure S2: Microfluidic setup. **a**, Setup for the bistable circuit. The contents of 3 aqueous channels are mixed according to the schematic pressure profiles shown on the left. The pressures are set to explore a square in the (P1,P2) space while P3 is adjusted to keep the sum of pressures constant in order to maintain monodispersity of the droplets. The role of P1 and P2 are inverted to symmetrize the exploration and reduce systematic biases. The script is repeated until enough droplets have been produced. Mix1 in channel 1 contains the master mix (all reagents except autocatalytic templates) plus the template αtoα and the red fluorescent barcode (Alexa647 labeled dextran). Mix2 in channel 2 contains the master mix plus the template βtoβ and the blue fluorescent barcode (Cascade Blue labeled dextran). Channel 3 contains Mix3, *i.e.* the master mix adjusted with water (as well as basal levels of barcodes to improve the linearity of detection at low concentrations, see method section) **b**, Because of the total pressure constraint, the zone explored in pressure space (P1, P2, P3) is necessarily contained in the P1+P2+P3 = constant plane, but can be an user-defined fraction of this simplex. **c**, Here, we have designed the pressure scanning protocol in such a way that projection in the space (P1,P2) yields a square, as well as two horizontal and vertical axes extending to pure Mix1 and pure Mix2. These serve for calibration purpose when converting barcode intensities (in arbitrary fluorescent units) to actual concentrations of the molecular species. **d,** Setup for the predator-prey system. Four channels are used (for exonuclease, polymerase, template and volume compensation). The pressures are set to follow a scripted random walk in the space (P1, P2, P3) in order to maximize coverage. **e**, Projection in the (P1, P2, P3) space gives a cube plus 3 calibration axes.

S1.3 Chamber preparation and imaging

The droplet emulsion was collected through a tip planted in the outlet. After generation, excess of oil was removed and the emulsion transferred to a 200 µL PCR tube. Droplets were sandwiched between glass slides to form a monolayer. The incubation/observation chamber consisted of a thick glass slide for the bottom (Matsunami Micro slide glass 76 mm × 52 mm, thickness ∼0.8-1.0 mm), and a thin cover slide for the top (Matsunami Micro cover glass 22 mm × 24 mm, thickness ∼0.12-0.17 mm). Bottom and cover slides were rendered hydrophobic to prevent droplet merging by spin coating a 10% dilution of Cytop CTL-809M (diluted in the provided solvent, Asahi glass) at 500 rpm for 5 seconds then 2000 rpm for 30 seconds. The freshly coated glass slides were then baked at 180 ºC for 60 minutes. We used glass beads (Polysciences Inc.) - filtered at 50 µm to match the size of droplets - as spacers to control the thickness of the chamber and prevent the formation of multilayers of droplets. To rigidify the chamber and avoid bending of the thin top slide (which would compromise the spatial homogeneity of the imaging), we poured a photo-curable adhesive (NOA81, Norland Products Inc.) on the spacers. We also added several drops of NOA on the periphery of the bottom slide. Lastly, to enhance droplet filling and prevent air bubbles, we applied ∼10 µL of NOA on two parallel edges of the chamber. We then cured the construct with an UV trans illuminator for 1 minute. The resulting chamber was filled by capillarity with ∼25-30 uL of droplet emulsion, closed with NOA and UV cured again (the emulsion was protected from UV exposure by an aluminum foil). Finally, we sealed the chamber with Araldite Rapid (Araldite Professional Adhesives) to improve long-term air tightness.

Droplets were imaged with a confocal laser microscope (Olympus Fluoview FV1000) mounted on a IX-81 chassis and equipped with a xy stage Optosigma Bios-206T, 4 lasers (405, 473, 559 and 635 nm) and a 20x (NA=0.75, bistable switch) or 10x (NA=0.40, predator prey) objective. The droplet chamber was incubated on stage with a transparent heat plate Tokai Hit MAT-1002ROG-KX. Droplets were imaged either at room temperature (bistable switch, after incubation at 42°C) or at 45°C (predator-prey oscillator, time lapse). The sample was turned upside down to reduce the number of glass layers in the optical path, and the total thickness [8]. For time-lapse, the scanning period was 6 minutes and the microscope was covered with a black sheet to reduce temperature fluctuations and stray light. After scanning, images were stitched by the Olympus software.

Table 2 shows the conditions of acquisition for confocal microscopy.

Experiment			BD 01: [β]>[α]	BD 10: [α]>[β]	1D scan	Predator-Prey
Resolution (pixel)			512 x 512	512 x 512	320 x 320	512 x 512
Objective mag. (N.A.)			20x (0.75)	20x (0.75)	20x (0.75)	10x (0.40)
C.A. (µm)			120	120	120	120
Lasers	405 nm	%	40	40	-	30
		PMT (V)	708	708	-	790
		VBF	425-460 nm	425-460 nm	-	425-460 nm
	473 nm	%	30	30	55	27
		PMT (V)	740	755	720	553
		VBF	495-555 nm	495-555 nm	495-555 nm	495-555 nm
	559 nm	%	30	30	30	27
		PMT (V)	644	644	659	641
		VBF	BA575-620	BA575-620	BA575-620	BA575-620
	635 nm	%	20	20	10	25
		PMT (V)	668	596	595	584
		VBF	BA655-755	BA655-755	BA655-755	BA655-755

Table 2: Acquisition parameters for confocal microscopy. The percentages indicate the laser power, "C.A" refers to the confocal aperture "PMT (V)" to the voltage of the photo-multiplier tube and "VBF" to variable barrier filter.

For the results shown in Fig. 3, scanning time was not a limitation (endpoint) and we scanned a large portion of the droplet chamber in order to compute a flat-field correction and reduce vignetting. To that end, we scanned, averaged and gaussian filtered ∼200 fields of view, which yielded a correction mask whose maximum intensity was set to 1 in each channel. We then divided pixels-by-pixels and channel-by-channel the scanned fields of view by their correction masks to compensate vignetting.

S1.4 Image processing

Images were processed in Mathematica. We describe first the processing of the bistable system data.

First, we individually detected droplets (Fig. S3). We segmented the TAM channel because of its high signal-to noise ratio and its bimodal distribution of intensities. We first applied a Gaussian filter with a radius of ∼70% the droplet radius. We then applied the *MaxDetect* function, which gives an image consisting of the extended maxima (sets of connected pixels brighter than their surrounding). We then applied a Gaussian filter of a few pixels and detected morphological components, which yields the centers of the droplets. We removed centers which were too close to their neighbors or located near the image borders. We then extracted the intensities of the 4 fluorescence channels by integrating over the whole droplet.

Processing of fluorescences: We then manually rescaled fluorescences. We used the apexes of the calibration axes (Fig. S16a) to convert (Alexa, Cascade) into concentrations (αtoα, βtoβ) (we discard negative concentrations). We then normalized TAM by manually defining the minimum TAM intensity to 0 and the maximum intensities to 1. We discarded droplets lying outside those bounds. We similarly normalized FAM by manually defining its minimum intensity to 1 and its maximum intensities to 0 (FAM shifts inversely with α). (Note that in Fig. 3d right, virtually all droplets are in a low FAM state. We set the FAM shift peak close to 1 and normalized its width with that of Fig. 3d middle) We do not attempt to convert FAM and TAM intensities to concentrations of α and β, the relationship between them being monotonic but non linear. Indeed the fluorescence shift saturates when the triggers exceed their binding Km (˜100 nM), the threshold being probably lower due to the stabilizing effect of stacking interactions or elongation by the polymerase). This indirect and saturating reporting is sufficient to distinguish a high state from a low state as demonstrated by the bimodality of the fluorescence histogram (Fig. S16). This whole processing generated a set of points in a 4D space (αtoα, βtoβ, FAM, TAM) that is projected into the 2D space (αtoα, βtoβ) to yield the raw bifurcation diagram (the color of a point indicating the level of FAM and TAM).

Smoothing and thresholding: We smoothed those raw diagrams by taking for an arbitrary point (αtoα, βtoβ) the local median (FAM,TAM) of its 20 nearest neighbors in parametric space (Fig. 3c,d). For Fig. 3c, we thresholded the (FAM,TAM) intensities to exploit the bimodal nature of their histogram. Intensities that are within ∼one standard deviation of the high (low) peak are assigned a value of 1 (0). Intensities that lie in-between are rescaled continuously between 0 and 1.

For the predator prey system (Fig. 4), some droplets displayed very little signals in all their fluorescence channels. Those "invisible droplets", located near the origin in the parameter space, contained very little template, exonuclease and polymerase. Since the template also serves to report on the level of preys, their observable channel was also dark and could not be used directly for morphological detection. We therefore used a two steps procedure to extract the coordinates of these droplets' centers:

- First, the previous localization method was applied to all four channel images of a given time point. The corresponding clouds of points were combined, clustered, and for each cluster, only the point associated with the brightest pixel was kept (this implies that for each droplet we used the brightest channel to detect the center). However, some droplets lying very close to the origin in barcode space (hence dark in all channels) were missed by this procedure.

- To avoid possible bias introduced by systematically omitting a particular area of the parameter space, we used a reconstruction step that leveraged the highly crystalline arrangement of droplets in the image: all detected droplet centers were converted to a disk with a radius equal to 90% of the average droplet diameter (computed using all already discovered droplets). This created a black and white image, which was subsequently blurred using a Gaussian filter. We could then apply the *MaxDetect* function to detect the center of the white areas, which was taken as an approximation of the position of the missing droplets. This graphical procedure was fast enough, and we manually checked that it indeed discovered most "dark" droplets (adding approx. 3% to the total number of detected droplets in a set of images). The complete process was then repeated for each 798 four-colors frames of the timelapse movie.

We then tracked the droplets to reconstruct their fluorescence time-traces. We adapted classical tracking algorithms to cope with the large size of our data set. For each frame n, we detect the droplets' centers (x_i, y_i) as indicated above. We then supplemented this vector with a barcode intensity vector, which gives for each frame a set of 3D points $p_i(n) = (x_i, y_i, barcode_i)$. The barcode is rescaled to be of the same magnitude than the spatial positions. In the case of the predator prey, we use the three barcodes. We built the droplet trajectories by recursively linking the $p_i(n)$: the successor of point $p_i(n)$ in frame n is simply defined as the nearest point $p_j(n+1)$ at frame $n+1$.

In other words we do not attempt to minimize the total deviation of centers between frames, which allows tracking to be parallelized and significantly sped up. This choice is justified by the fact that droplets move very little, and that the barcode dimension further decreases tracking errors. We then remove trajectories with large jumps and verify on randomly selected droplets the correctness of tracking.

Once we had a trajectory associated to each droplet, we could extract the fluorescence time trace by taking droplet-averaged fluorescence values as above. These time traces were smoothed (moving average over 8 frames) and detrended using the built-in Mathematica functions. Peak positions and heights were then detected using the *FindPeak* function and used directly to compute the oscillation score.

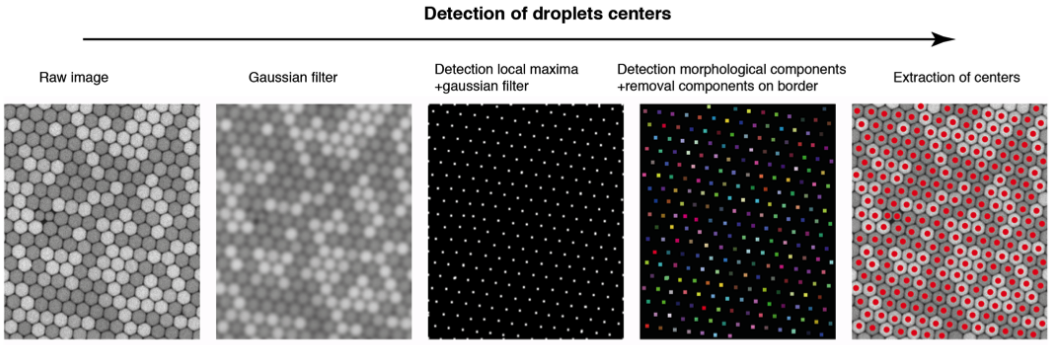

Figure S3: Extracting the centers of droplets. The raw image is first smoothed with a gaussian filter. Local fluorescence maxima (roughly a small rectangle located around the brightest point of each droplets) are then detected and smoothed slightly (note that the local maxima are enlarged for sake of clarity in this figure). The resulting image is then segmented to provide morphological components, centroids of which are used as centers of droplets.

S1.5 Content of supplementary files

- **Droplet array for the bistable switch (Alexa channel)**: This image shows the fluorescence in the Alexa channel of an array of droplets generated for the experiment on the bistable switch. It corresponds to the image in section section S10 of this Supplementary Material.
- **Droplet array for the bistable switch (Cascade channel):** This image shows the fluorescence in the Cascade channel of an array of droplets generated for the experiment on the bistable switch.
- **Droplet array for the bistable switch (FAM channel):** This image shows the fluorescence in the FAM channel of an array of droplets generated for the experiment on the bistable switch.
- **Droplet array for the bistable switch (TAMRA channel):** This image shows the fluorescence in the TAMRA channel of an array of droplets generated for the experiment on the bistable switch.
- **Chip design:** This CAD file contains the Autocad source for the chip design.
- **Movie 1:** This movie shows the scanning of inlet pressures near the microfluidic junction. Channels contain fluorescence dyes for visualization. Note that the script has been slowed down to facilitate recording.
- **Movie 2**: This time-lapse movie shows the fluorescence of droplets in the TAMRA channel. The variable t denotes the frame number.
- **Movie 3:** Example of sustained and bursting oscillations.
- **Pressure script used for Bistable switch:** This Autoit file contains the script used for generating the pressure profiles in the bistable switch experiment
- **Pressure script used for predator prey:** This Autoit file contains the script used for generating the pressure profiles in the Predator Prey experiment.

S2 Estimation of barcode diffusion during droplets generation

The concentration of a template or enzyme is encoded by the fluorescence of a dextran barcode. It is therefore primordial that their concentrations remain proportional during generation, incubation and scanning of droplets. Although laminar flows do not mix by convection (due to the low Reynolds number of microfluidic flows), reagents can diffuse between them. Because the diffusion coefficients of DNA templates and dextran barcodes are not equal, diffusion may add noise to the reading of concentrations. It is therefore important to estimate the prevalence of diffusion occurring when different aqueous channels contact each other before the partitioning in droplets (Fig. S4).

To set ideas, we assume a (conservative) droplet generation rate of 100 Hz. The higher the flow rate, the higher the prevalence of convection over diffusion, and thus the lower the noise added by the differential diffusion of templates and barcodes. We assume diffusion coefficients for dextran of $22\,\mu m^2/s$ and for DNA $53\,\mu m^2/s$ [9, 10]. The length scale L over which a species with a diffusion coefficient D diffuses during a time t is $L = \sqrt{Dt}$.

When the flow rate of a channel becomes negative (due to low pressure), it is invaded by another channel. During this time, the fronts of the invaded and invading channels come into contact and exchange reagents by diffusion (Fig. S4). Conservatively assuming an invasion lasting 10 seconds, the barcode will have diffused over a length scale of 15 µm and the DNA template over 23 µm, which is less than half the diameter of a droplet. However 1000 droplets will have been generated simultaneously from the other channels with a positive flow rate. So diffusion during invasion should be negligible.

Once templates and barcodes are encapsulated into a droplet, diffusion becomes drastically slower, hindered by the continuous oil phase that separates water droplets. Estimates for transport of reagents between droplets are harder to obtain. Yet, previous papers using a similar surfactant did not observe significant transport of labelled DNA templates between droplets [8, 11, 12]. Lastly digital PCR is routinely carried out with this surfactant [13], which indirectly confirms the impermeability of droplets to DNA. Overall, these predictions are confirmed experimentally in section S4.

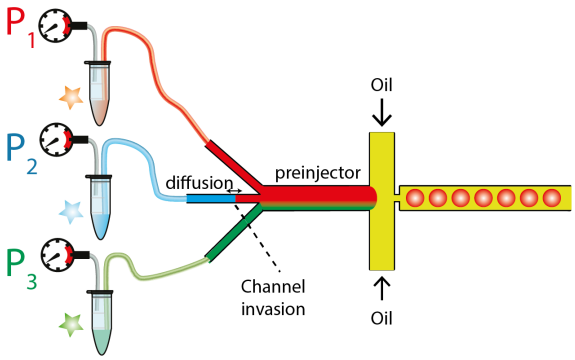

Figure S4: Possible sources of barcoding discrepancy. During invasion of a channel by another one, reagents can diffuse between flows, leading potentially to noise in barcoding.

S3 Scaling of the platform

In this section we discuss the scaling of our microfluidic platform. How far can we push this technology? How many parameters can we scan? Generation of droplets - although serial - is not an immediate bottleneck. We routinely generate ∼1 million of droplets in ∼45 min, and faster rates of 1 MHz have been achieved in the literature [14] (although without combinatorial preparation). Programming the pressure profiles to mix more than 4 inlets would require care, but should not be beyond reach. Incubation of droplets is not a bottleneck since reactions run in parallel. Fluorescence scanning of the droplets proves to be the most time-consuming operation. We chose confocal laser microscopy because of its high signal-to-noise ratio. But this scanning method is serial and thus slow. Scanning $\sim$ 10000 droplets requires about $\sim$ 5 minutes. Faster rates could be achieved by decreasing the scanning resolution and the time spent on each pixel, pushing up the laser power if needed to compensate for the lower number of photons collected per droplet. Faster methods of scanning could also be considered. Droplet flow cytometry (a sequential method) scans $\sim$ 2000 droplets/s ($\sim$ 600000 droplets/ 5 min) [15]. Among parallel acquisition methods, a sCMOS camera coupled with epifluorescence microscopy is an attractive option. A 5 megapixel sCMOS camera

can nominally scan $\sim$ 50000 droplets simultaneously at a resolution of 100 pixels/droplet. Assuming an acquisition time on the order of 10 seconds per frame (including stage translation, filter switching and exposure), a sCMOS setup will record the fluorescence of 1.5 million droplets per 5 minutes. Note that parallel scanning methods require more careful calibration than sequential ones to account for the spatial dependence of the illumination and sensors. Fluorescence overlap will also have to be dealt with, but it is realistic to encode the concentration of 6 variables simultaneously [16]. For example in the case of the bistable switch, this would give 4 parameters (two autocatalytic templates and two initial concentrations of triggers) and two observables (steady state level of triggers), thus providing in a single experiment not only the complete 2-dimensional bifurcation diagram, but also the basins of attraction corresponding to each parameter set.

S4 Relative precision of barcoding

Here we estimate the relative errors associated with using labelled dextran as barcodes. In our barcoding strategy, the fluorescence intensities of dextran are taken as a proxy for the concentrations of a non fluorescent parameter species (DNA template or enzyme) that has been co-encapsulated. Yet dextran are branched polysaccharides whose physico-chemical properties (charge, diffusion coefficient...) differ from their surrogate species. We performed the following experiment to assess the reliability of labelled dextran as barcodes. We prepared two mixtures, each containing a labelled dextran and a labelled DNA strand (Fig. S5a). We then generated droplets containing r% of the mixture 1 and $(100-r)$% of mixture 2, with r taken between 0 and 100. This experiment recapitulates various sources of microfluidic noise that could affect the barcoding precision.

The mixture 1 contains Cascade Blue-labelled dextran (5 nM), Alexa 647-labelled dextran (100 nM), the FAM-labelled $\alpha toi\beta$ (100 nM), and the TAMRA-labelled $\beta toi\alpha$ (10 nM). The mixture 2 contains Cascade Blue-labelled dextran (200 nM), Alexa 647-labelled dextran (20 nM), the FAM-labelled $\alpha toi\beta$ (10 nM), and the TAMRA-labelled $\beta toi\alpha$ (100 nM). The buffer contains 20 mM Tris-HCl, 10 mM $(NH_4)_2SO_4$, 10 mM KCl, 50 mM NaCl, 8 mM $MgSO_4$, 0.1 % Synperonic F108, dNTPs (400 µM each), 2 µM Netropsin, 3 mM DTT and 500 µg/ml BSA. The droplets are scanned at room temperature after generation in conditions similar to the main paper (512x512 pixels per field of view, 20 µs/pixel, CA 120 µm, zoom 1x, objective 20x (NA0.75)).

Figure S5b shows the scatter plot of fluorescences. As expected, the intensities of dyes coming from the same microfluidic channel are strongly correlated, while dyes coming from different channels are anti-correlated. More precisely, we can estimate the (relative) reading errors associated with measuring the fluorescence of dextran markers instead of their surrogate DNA strands. Using Mathematica we perform a linear regression to extract the coefficients of variation. For (Cascade Blue Dextran, TAMRA-labelled DNA) this error is $\sim$3%. For (Alexa Dextran, FAM-labelled DNA) this error is $\sim$4%. This experiment therefore confirms that labelled Dextrans can reliably barcode the concentration of DNA templates with a relative precision of a few percents. The experiment also shows that diffusion during droplets generation does not significantly add noise to barcoding, confirming the estimates of section S2.

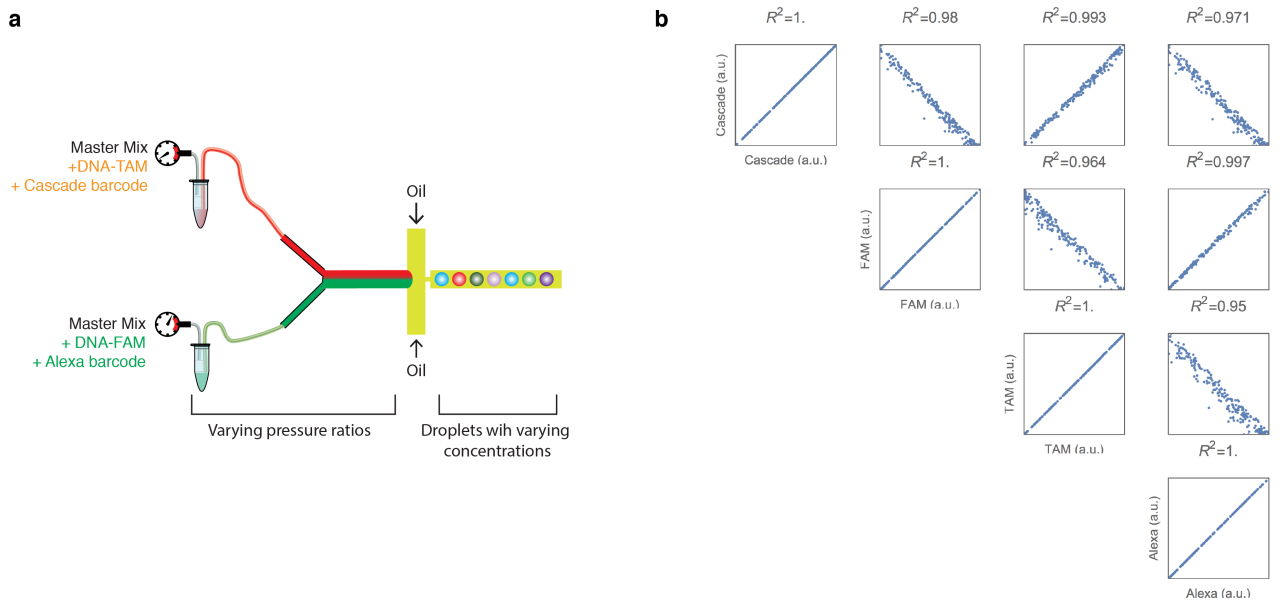

Figure S5: Measuring the relative barcoding errors. **a** Microfluidic generation of droplets with correlated contents. Each channel contains two fluorescent species: a DNA strand and a labelled dextran. The pressures of aqueous channels are varied between their minimal (channel invaded) and maximal (channel fills the pre-injector and invades the other channel) values while keeping their sum constant. **b** Scatter plots (in arbitrary fluorescence units) showing the correlation of the fluorescence dyes within a single field of view (N= 218 droplets).

S5 Thermodynamic analysis of strands in the bistable switch

This section shows a thermodynamic analysis of strands comprising the bistable switch done with Nupack [17]. It contributes to qualitatively explain the distinct replication strengths and behaviors of α and β. We computed the pairing fraction at equilibrium of the triggers and their templates (Fig. S6). Firstly, this ensemble plot (Fig. S6a) confirms the binding orthogonality of (α, αtoα) vs. (β, βtoβ) as seen from the absence of pairing in the corresponding region of the plot. Secondly, the trigger α preferentially binds to its template through the input position (downstream). On the other hand, β also binds preferentially to the input position, but the fraction of binding to the output position (upstream) is larger. Such bindings are unproductive (the trigger cannot be extended); β must detach from the output position and reattach to the input position for an output to be generated. Thirdly, the template αtoα does not possess stable secondary structures, while βtoβ presents a small hairpin with a double stranded neck of 3-4 basepairs (Fig. S6b). This hairpin structure sequesters the 3' end of βtoβ, which likely slows down the binding and extension of β strands. Overall these observations help to explain why replication of β appears slower than α, and thus the relative surface of the 01 and 10 zones.

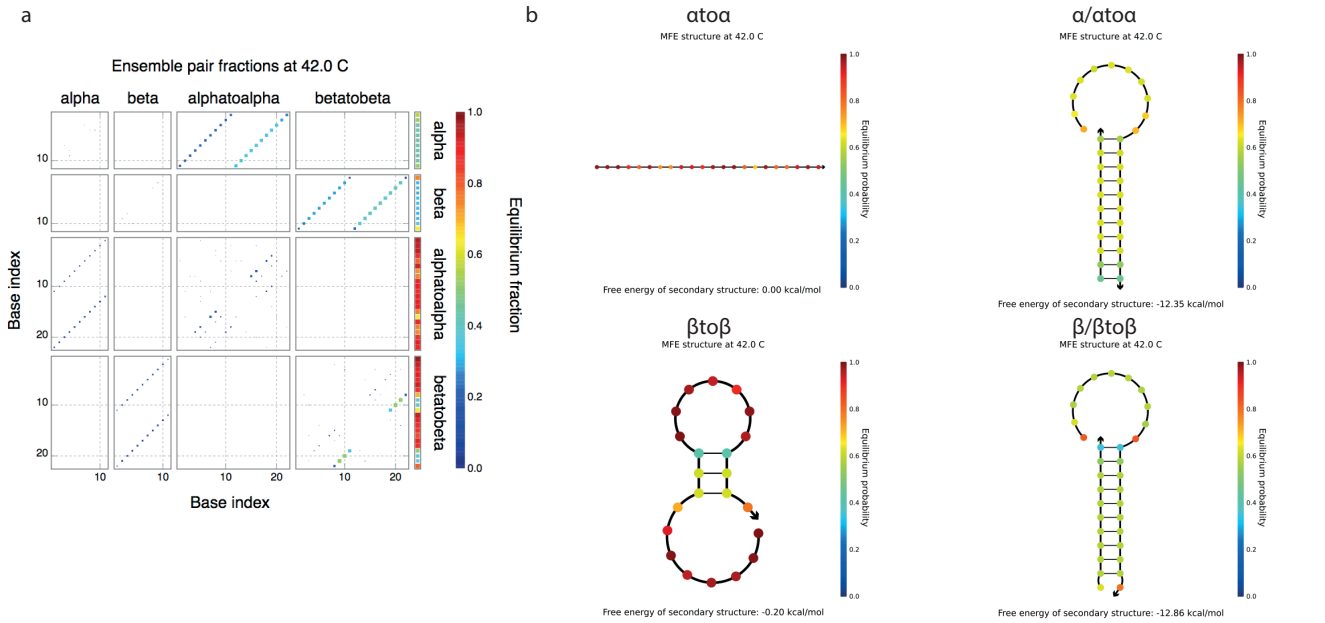

Figure S6: Thermodynamic analysis of the bistable switch. **a** Ensemble pair plot for a mixture of αtoα (200 nM), βtoβ (200 nM), α (50 nM) and β (50 nM). We use the following conditions: 42°C, 8 mM $Mg^{2+}$and 50 mM Na^{+}. Because Nupack cannot handle hybrid RNA/DNA polymer, U bases were replaced by T bases. **b** Minimum Free Energy structure for each complex.

S6 Biochemical orthogonality of dextran barcodes

To investigate the possible effects of labelled dextrans on the reactivity of the PEN DNA toolbox, we monitored a predator-prey system with increasing concentrations of dextran labelled with Alexa 647 or Cascade Blue (experiment performed in a CFX Real-Time PCR System thermocycler). We mix the grass template (5' C*G*G*CCGAATGCGGCCGAATG-dy530 3', 140 nM), the prey strand (5' CATTCGGCCG 3', 20 nM) and the predator strand (5' CATTCGGCCGAATG 3', 10 nM) in a buffer containing 20 mM Tris-HCl, 10 mM $(NH_4)_2SO_4$, 10 mM KCl, 50 mM NaCl, 8 mM $MgSO_4$, 0.1 % Synperonic F108 , 400 µM of each dNTP , 2 µM Netropsin , 1 eq. EvaGreen, 3 mM DTT, 500 µg/ml BSA and 5 µg/ml of ETSSB, 50 units.mL^{-1} Bst DNA Polymerase Full Length (NEB), 20 nM of ttRecJ exonuclease, 400 units.mL^{-1} Nb.BsmI, and 0 nM to 1 µM of each labelled dextran.

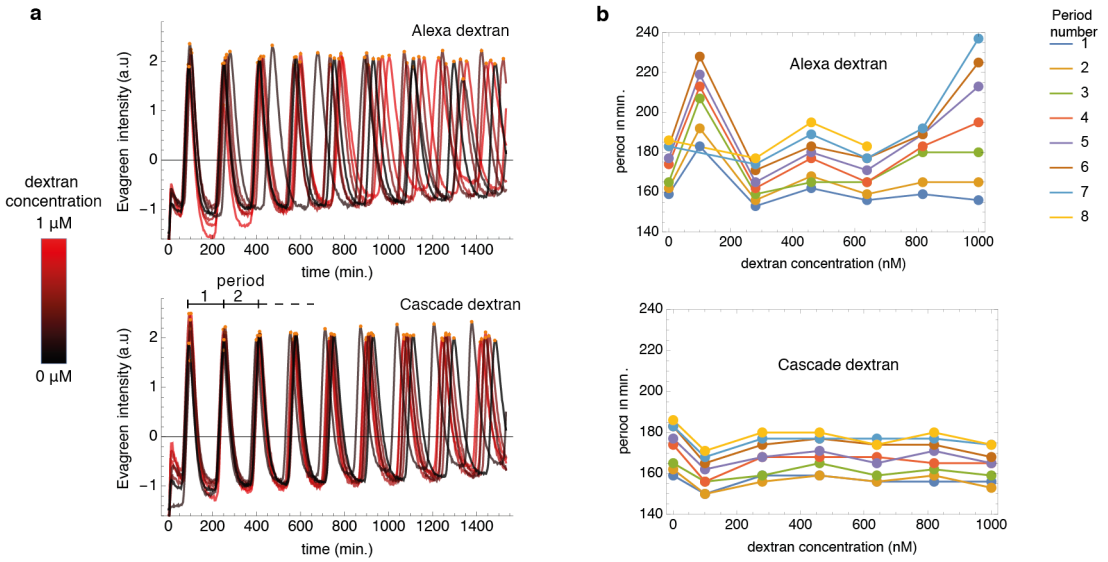

Figure S7: Chemical orthogonality of the dextran barcodes against the predator prey system. **a.** Fluorescence time traces against varying concentrations of labelled dextrans. The curves have been standardized (to compensate well-to-well variations) to have zero mean and unit standard deviation. The concentrations of dextran barcodes are 0, 100, 280, 460, 640, 820 and 1,000 nM. Note that the control at 0 nM (black trace) is replotted in each graph for sake of comparison. The orange dots indicate detected peaks (the number of peaks detected per trace varies as some fall near the experimental cutoff). **b.** From the peak times we extract the duration of the i^{th} period for each concentration of dextran. Again the control at 0 nM is plotted twice to ease comparison.

Results in Fig. S7 show that Alexa 647 dextran (up to 280 nM) and Cascade Blue dextran (up to 1000 nM) are orthogonal to the DNA biochemistry (except for an outlier at [Alexa dextran]= 100 nM which is likely due to a pipetting error or dust in the tube). The effect of Alexa 647 dextran becomes noticeable at concentrations over 800 nM, as shown by the widening of the periods' standard deviations (Fig. S7b).

S7 Estimating the 00 zone of the bistable switch

In this section, we show that assuming continuous dynamic and first-order amplification, we expect the 00 zone (the set of template concentrations that yield a null steady state) to be a rectangle independent of the initial concentrations of triggers (which we take to be strictly positive). Because we assume that the dynamic is continuous and deterministic, the concentration of a species that is initially strictly positive can never become identically null. We consider a simplified model that was validated experimentally (see [18]). Triggers are amplified according to a first-order Michaelis-Menten amplification whose rate is modulated by the concentrations of autocatalytic template, polymerase and the nickase. The triggers are degraded according to linear kinetics by the exonuclease:

$$\begin{aligned} \alpha' &= \frac{p_\alpha[\alpha to \alpha]\alpha}{K_\alpha + \alpha + i_\alpha} - k_\alpha \alpha \\ \beta' &= \frac{p_\beta[\beta to \beta]\beta}{K_\beta + \beta + i_\beta} - k_\beta \beta \end{aligned}$$

The constants p_α and p_β capture the overall replication rates of the triggers by the polymerase and nickase. The variables i_α and i_β are the concentrations of species inhibiting α and β respectively (whose kinetics need not be written explicitly here). The constant k_α and k_β encompass the degradation rates of the exonuclease.

For amplification of α to occur ($\alpha' > 0$), it is necessary that the level of autocatalytic template $[\alpha to \alpha]$ exceeds a threshold concentration $K_\alpha k_\alpha / p_\alpha$ (and similarly for β). This contrasts with second-order autocatalysis, where the concentrations of the initial catalyst and template must *both* exceed a critical threshold to ignite replication. In other words, the steady states $\alpha = 0$ or $\beta = 0$ are never stable in first-order amplification once the threshold is

crossed because any infinisitimal level of trigger will be amplified. Let us define the rectangle R_{00} in the parameter space ($\alpha to \alpha$, $\beta to \beta$) by

$$R_{00} = \{0 \leq \alpha to \alpha \leq K_\alpha k_\alpha / p_\alpha \ , 0 \leq \beta to \beta \leq K_\beta k_\beta / p_\beta\}$$

This rectangle is thus necessarily included in the 00 zone. Now we prove the reverse inclusion, namely that the 00 zone is included in the rectangle. Suppose that we start outside R_{00} (at least one template exceeds its threshold level) but that α and β both asymptotically decay to zero. Then the inhibitors also eventually decay to zero. After a (possibly long) relaxation time T_∞, we have β, $i_\beta \ll K_\beta$ and α, $i_\alpha \ll K_\alpha$ and thus

$$\begin{aligned} \alpha' &= (\frac{p_\alpha[\alpha to \alpha]}{K_\alpha} - k_\alpha)\alpha \\ \beta' &= (\frac{p_\beta[\beta to \beta]}{K_\beta} - k_\beta)\beta \end{aligned}$$

Given α and β are both non null (because of to their deterministic and continuous evolution), at least one species is amplifying (the species whose template exceeds its threshold concentration), which contradicts the assumptions that the system is converging toward the null state.

This simple model predicts that the 00 zone should be a rectangle whose shape is independent of the initial concentrations of triggers. Since this is clearly not the case in Figure 3, at least one of our hypothesis must be false. Firstly, the actual mechanism of replication may be higher-order, which would provide the necessary hysteresis to stabilize the steady state $\alpha = 0$ or $\beta = 0$. Secondly, the dynamic may not be fully continuous. The concentrations of α and β cannot be arbitrarily low without being null (40 fM × 65 pL ≈ 1 molecule). In their race against degradation, the autocatalytic templates may sometime lose and the copy numbers of α and β both reach and remain at 0 (something impossible in a well-posed, deterministic ODE because of the uniqueness of its solution). Since a template cannot replicate a strand that is absent, the 00 zone in our diagram may therefore represent circuits that are "stochastically trapped" in the null state 00. Lastly, when the levels of templates are close (but superior) to their thresholds, the relaxation may drastically slow down and exceed our experimental time scale (10 hours). This phenomenon would be reminiscent of critical slowdown, where some dynamic systems have been shown to take a very long time to recover from quasi-lethal perturbations [19].

S8 Mathematical analysis of the Predator Prey

S8.1 Scaling

Here we show from scaling arguments that the quantity $\mu = \frac{exo}{tem \times pol}$ plays a role in shaping the oscillatory region of the predator-prey system (Fig. 4 in the main paper). We consider a general kinetic model with 3 biochemical reactions of replication, predation and decay. For sake of generality, we do not assume much about their inner kinetics, except than their rates vary linearly with their catalysts concentrations. This encompasses most enzymatic models such as Michaelis-Menten, Hill cooperativity or competitive inhibition. We model the dynamics of preys and predators (noted $x(t)$ and $y(t)$ respectively) as follows:

$$\begin{aligned} \frac{dx(t)}{dt} &= tem \cdot pol \cdot f(x,y) - pol \cdot g(x,y) - exo \cdot h(x,y) \\ \frac{dy(t)}{dt} &= pol \cdot g(x,y) - exo \cdot l(x,y) \end{aligned}$$

The term $f(x,y)$ represents the replication of preys, mediated by the polymerase and the template. The second term $g(x,y)$ represents the predation reaction, mediated only by the polymerase. The last terms $h(x,y)$ and $l(x,y)$ represent the degradation of preys or predators by the exonuclease. Factorizing the equations by $tem \times pol$, we get:

$$\begin{aligned} \frac{dx(t)}{dt} &= tem \cdot pol(f(x,y) - \frac{1}{tem} g(x,y) - \frac{exo}{tem \times pol} \cdot h(x,y)) \\ \frac{dy(t)}{dt} &= tem \cdot pol(\frac{1}{tem} g(x,y) - \frac{exo}{tem \cdot pol} \cdot l(x,y)) \end{aligned}$$

Now we define the reduced constants $\mu = \frac{exo}{tem \cdot pol}$ and $\eta = 1/tem$. We also define a time-rescaled variable x' by $x'(t) = x(\frac{t}{tem \cdot pol})$ (and similarly for y and y'). We obtain the reduced system:

$$\begin{aligned} \frac{dx'(t)}{dt} &= f(x', y') - \eta g(x', y') - \mu h(x', y')) \\ \frac{dy'(t)}{dt} &= \eta g(x', y') - \mu l(x', y') \end{aligned}$$

This reduction shows that the dynamics of droplets with identical μ and η will be identical modulo an individual rescaling of time. In other words, droplets with identical (μ,η) in the oscillatory region will oscillate with a period proportional to $\frac{1}{tem \cdot pol}$.

S8.2 Linear Stability analysis

In this section we use a modification of the simple two-variable mathematical model introduced in [20]. The analysis is similar to the previous one and is only briefly sketched here. The two-species model was derived from basic considerations of the underlying kinetic mechanism as recapitulated in Fig. S8 and has been shown to provide a reasonable description of the experimental time traces for bulk experiments. The concentration of prey is noted N, that of the template is G, and the concentration of predators is P.

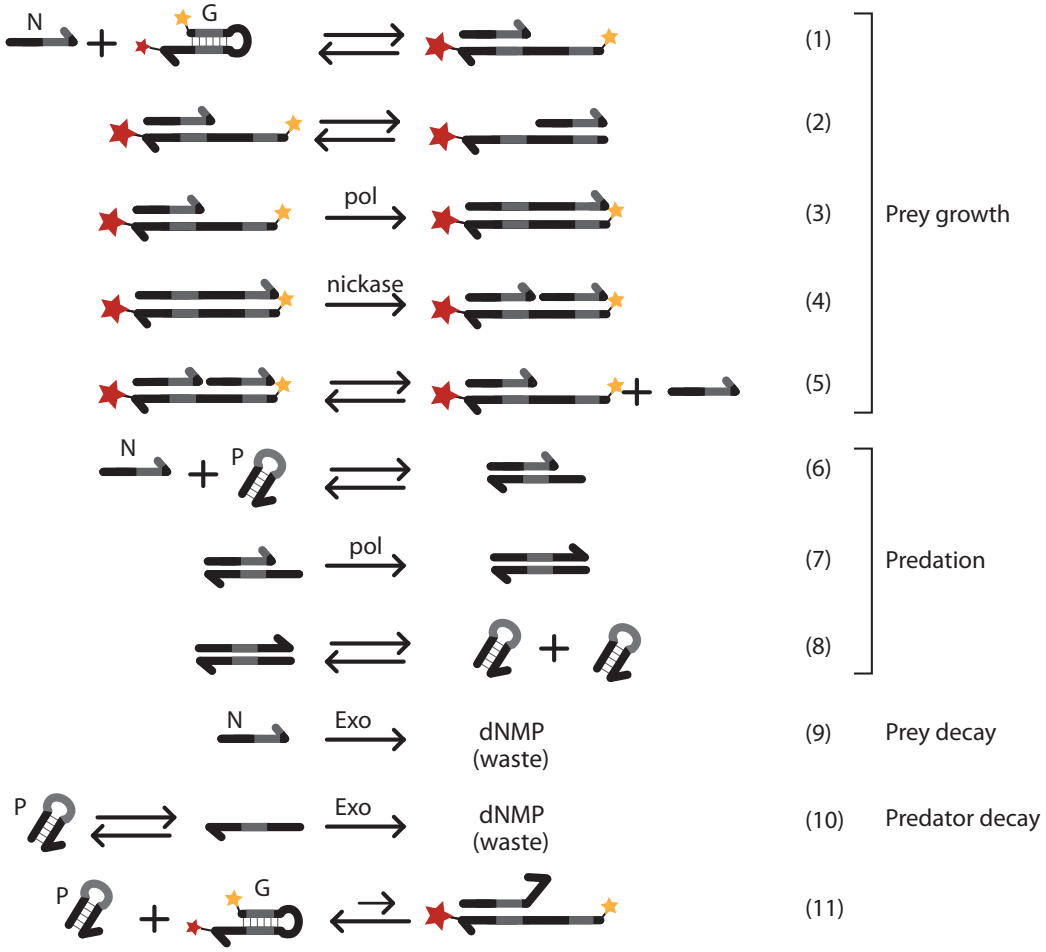

Figure S8: Full reaction network of the predator-prey system. Gray and black parts in the strand sequences emphasize the building of the predator palindrome, not sequence domains. The stars represents the template-bound TAMRA and JOE fluorescent dyes, their size being related to the fluorescence intensity. This diagram is adapted from [20]. N indicates the prey, P the predator and G the template.

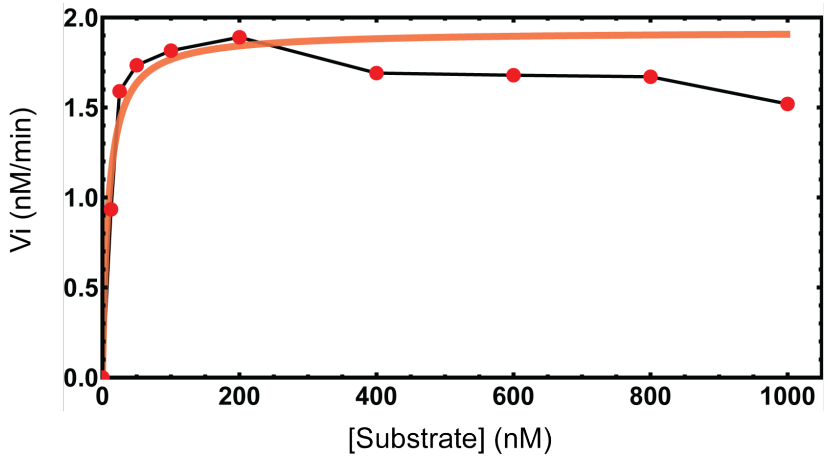

Figure S9: *Michaelis-Menten plot for the nicking enzyme Nb.BsmI at 10 U/mL.* The enzyme was incubated at 45 °C in buffer with various quantities of a fluorogenic hairpin substrate (Cy5-*G*T*C*A**GAATG-C**TCG –AGAC-TTTTT-GTCT-CGA**G-ˆCATTC**TGAC-BHQ2; recognition site in bold and nicking site indicated by ˆ, * are phosphorothioate modifications), and the initial rate was monitored by comparison with a standard. For fitting to the Michaelis-Menten equation (orange curve), the last 3 points were omitted, because they seemed to be affected by some form of non-Michaelian inhibition. The fitted parameters are $Vm_{@10u/mL} = 1.9\,nM/min$ and $Km = 9\,nM$

The assumptions used to reach the 2-variable model are sketched briefly below:

- The polymerase and exonuclease are processive enzymes, and their reactions can be considered as individual chemical events.
- Binding of G and P to the prey is weak. It thus becomes possible to consider that the amount of duplex species is always a small fraction of the total population of each P and N species, and approximate them as $K_P.P_{tot}.N_{tot}$ and $K_G.G_{tot}.N_{tot}$.
- The polymerase works mostly in the first order regime.
- Degradation is a competitive process between prey and predator, where predators have a much lower K_m and V_{max}.
- In addition to the previous results, we have measured the kinetics of the nicking enzyme Nb.BsmI and found a Michaelis-Menten form with V_m below $2\,nM/min$ at 10 U/mL. Considering this low rate, it seems reasonable to assume that the prey production reaction bottleneck is mostly the nicking event, and the previous steps are in the first order regime. Hence we write, noting $\varphi_{N\triangleright N}$ the reaction flux producing new preys (*i.e.* the kinetic term associated with production):

$$\varphi_{N\triangleright N} = k_1 \cdot pol \frac{G \cdot N}{1 + b \cdot pol \cdot G \cdot N} \tag{1}$$

where k_1 and b are empirical kinetic parameters controlling, respectively, the first-order kinetic rate of the reaction (at low substrate levels), and the saturability of the process ($\frac{1}{b \cdot pol}$ being equivalent to the Michaelis-Menten constant of the pathway). The difference with the derivation in [20] is the introduction of the polymerase in the saturation parameter of the denominator.

Following the previous results and noting *pol*, *tem* and *exo* for the non-dimensionalized concentrations of the three enzymes, we obtain the differential equations:

$$\frac{dn}{d\tau} = \frac{pol \cdot tem \cdot n}{1 + \beta \cdot pol \cdot tem \cdot n} - pol \cdot p \cdot n - \lambda \cdot exo \frac{n}{1+p} \tag{2}$$

$$\frac{dp}{d\tau} = pol \cdot p \cdot n - exo \frac{p}{1+p} \tag{3}$$

Analytical treatment is not directly possible for these equations, but can be performed for the mildly saturating case (i.e. when $\beta \cdot pol \cdot tem \cdot n$ is always small compared to 1). In this case, the first equation can be approximated as:

$$\dot{n} = pol \cdot tem \cdot n(1 - \beta \cdot pol \cdot tem \cdot n) - pol \cdot p \cdot n - \lambda \cdot \delta \frac{n}{1+p} \quad (4)$$

Bifurcation analysis

By setting $\dot{n}$ and $\dot{p}$ to 0, one finds four equilibrium points:

- (0, 0) *i.e* extinction of both species,
- $(\frac{tem.pol - exo \cdot \lambda}{\beta \cdot pol^2 \cdot tem^2}, 0)$ *i.e.* extinction of the predator and stable population of prey, valid for $\lambda \cdot exo < tem \cdot pol$ (*i.e.* first order production rate of preys overcomes their decay)
- $(\frac{1+tem+\sqrt{\Delta}/pol}{2(pol \cdot tem^2 \cdot \beta + \lambda)}, -1 + tem - \frac{\sqrt{\Delta}}{2pol})$, corresponding to coexistence of both species, valid for $tem > 1 + \frac{\sqrt{\Delta}}{2pol}$ and $\Delta > 0$.
- $(\frac{1+tem-\sqrt{\Delta}/pol}{2(pol \cdot tem^2 \cdot \beta + \lambda)}, -1 + tem + \frac{\sqrt{\Delta}}{2pol})$, also corresponding to coexistence of both species.

with $\Delta = \sqrt{(pol - pol \cdot tem)^2 - 4pol(-pol \cdot tem + exo \cdot pol \cdot tem^2 \beta + exo \cdot \lambda)}$. By looking at the eigenvalues of the community matrix linearized around these points (see [21]) we find that:

- the first point is stable for $\lambda \cdot exo > tem \cdot pol$.
- The second point is stable for $\lambda \cdot exo < tem \cdot pol$ and $\lambda \cdot exo > tem \cdot pol(exo \cdot tem \cdot pol - 1)$.
- The third is never stable over its domain of existence.
- The fourth has an unstable region (corresponding to the oscillatory area) and a stable region (corresponding to damping oscillations). These areas are defined by complicated analytical expressions.

We can then use the analytical forms to compute the theoretical bifurcations diagram. The results are schematized in Fig. S10. Two dimensional slices in {*pol*, *exo*} and in {*pol*, *tem*} are shown in Fig. S11.

The slices obtained in Fig. S11 reproduce the features of the experimental diagram: the oscillating area is observed below a $exo/pol = cste$ line in the *tem* slices and beyond a $pol \cdot tem = constant$ hyperbola in the *exo* slices. The oscillating region decreases in size and migrates toward the axis with increasing *tem* or increasing *exo*. For higher *pol* values, the limit cycle gives way to a fixed stable point, and thus a damping behavior is expected for most initial conditions. For a given set of *exo* and *tem*, Fig. S12 shows the behavior when one increases *pol*, starting from the extinction area: oscillations appear suddenly, become faster and then evolve to damped oscillations leading to a stable asymptotic state. The "oscillation score" profile can be computed and shows the asymmetrical shape also observed experimentally.

Another observation is that, when *tem*, *pol* and *exo* are not too large, the Hopf bifurcation delineating the region of stable limit cycles is almost merged to the boundary of the (0,0) area. As shown above, the equation defining this particular surface is $\lambda \cdot exo = tem \cdot pol$. We thus recover the scaling discussed theoretically above, and obvious from the experimental results. This also suggests that the sharp boundary observed in the experimental diagram on the low *(pol, exo, tem)* side is indeed a Hopf bifurcation.

Finally, we see that in some cases, the region of stable oscillations can coexist with another stable point, either the extinction state (yellow) or the prey-only (pink) state. This would define a so-called "hard-excitation" system, having two asymptotic attractors, one being a fixed point and the other a limit cycle. Given some noise, such a system would be able to switch spontaneously between cycling and flat behavior. This would happen however on a very limited parameter range, located precisely at the interface between the limit cycle area and the extinction zone (*i.e.* close to the Hopf bifurcation). Indeed, if we numerically solve the two-variable ODE system with a noise component (Langevin dynamic) within this multimodal region we observe a bursting behavior similar to the experimental results (Fig. S13).

Globally, linear stability analysis of a very simple two-variable model is in good agreement with the shape of the experimental diagram. It confirms that we do experimentally observe the Hopf bifurcation on the low concentration side, while its exact position on the other side is masked by the existence of damped trajectories. The effect of

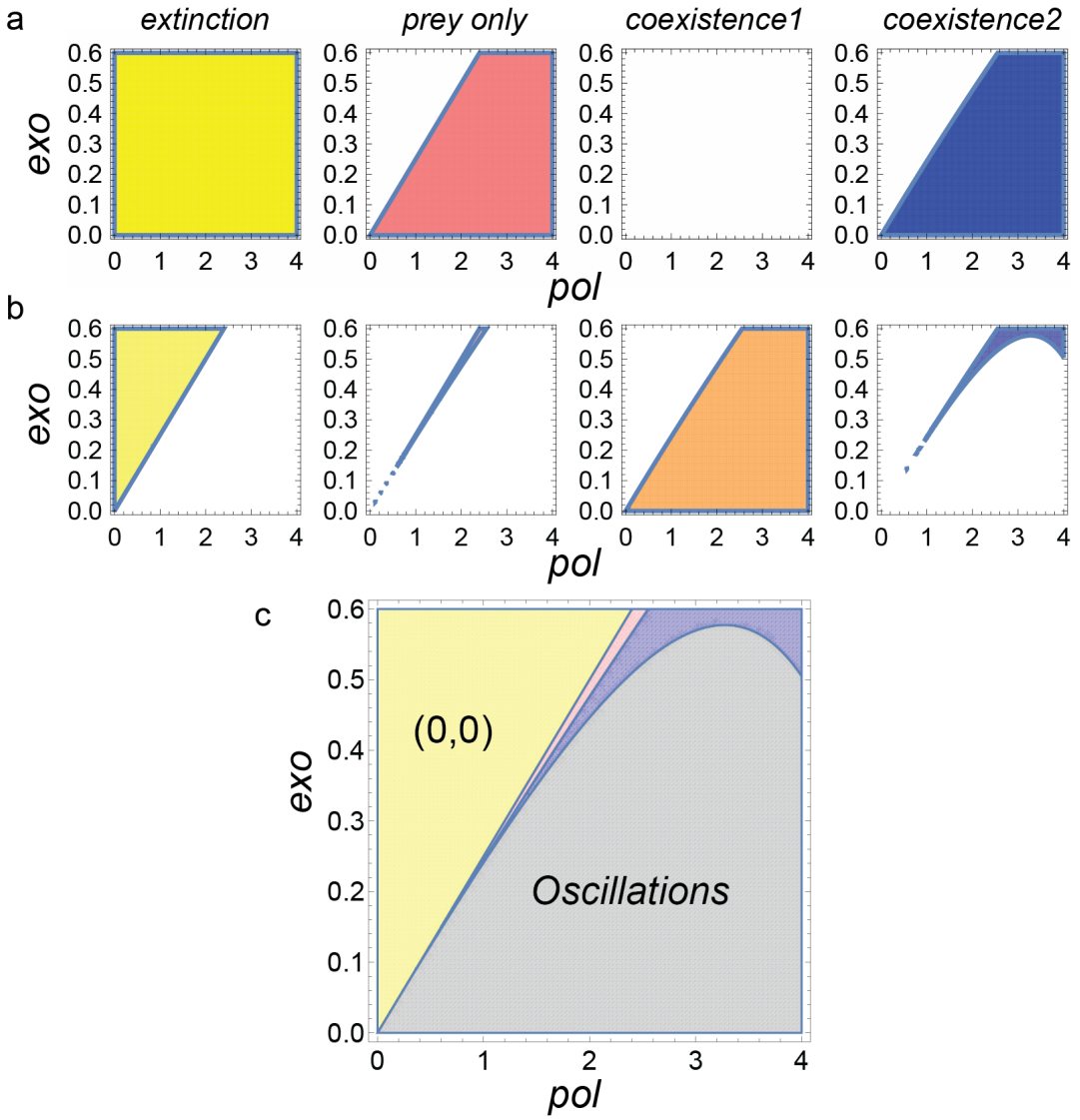

Figure S10: Bifurcation analysis of the model defined by equations 3 and 4. β and λ are set to 0.1 and 4, respectively (see reference [20]). *tem* is set to 1. **a**, Regions of existence of *positive* solutions. **b**, Stability of solutions. **c**, Bifurcation diagram showing the Hopf bifurcation around the oscillatory region (in gray). Yellow corresponds to the extinction region (no prey, no predators), pink to the prey-only area, and blue to the stable coexistence area.

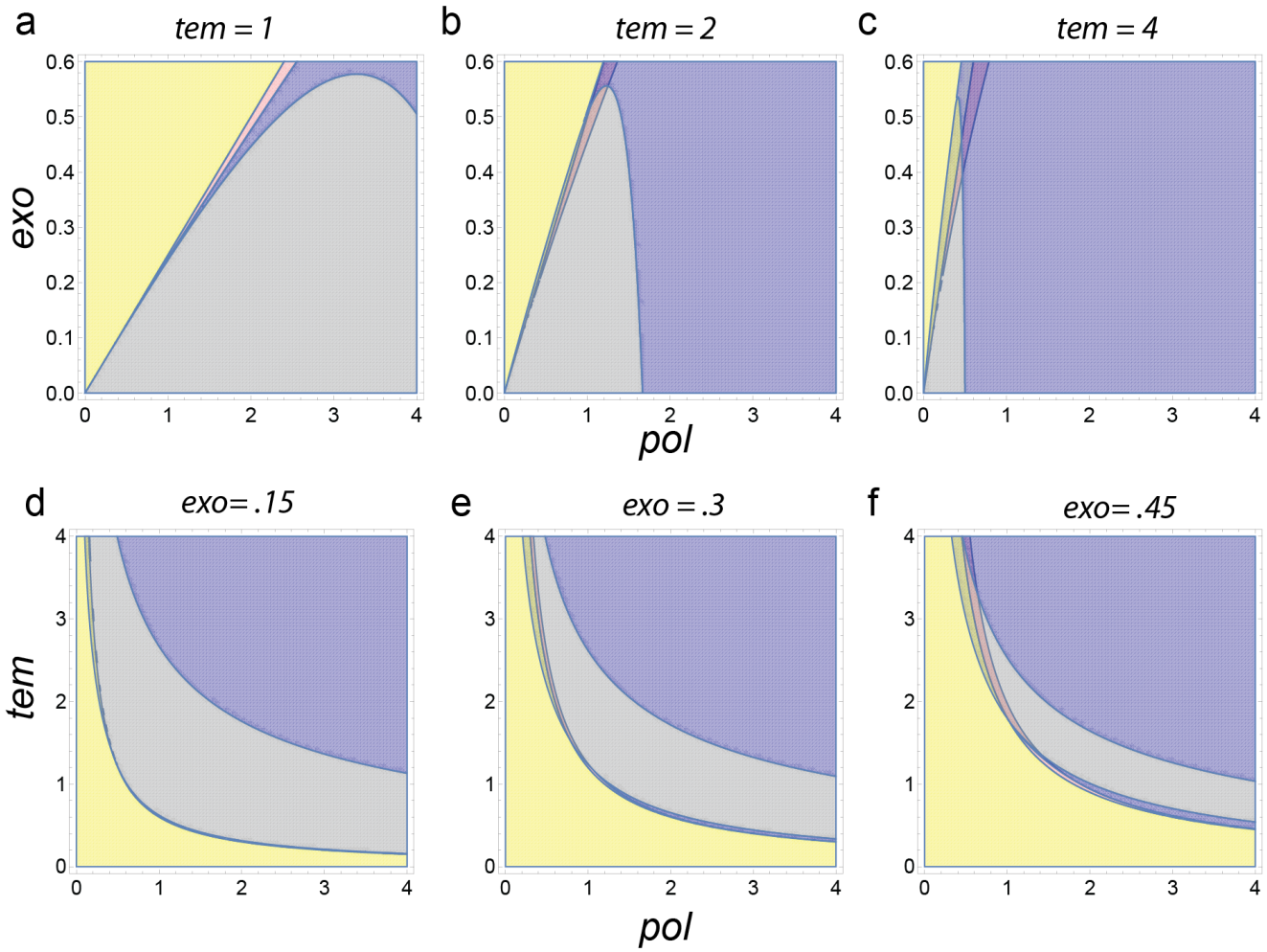

Figure S11: 3-dimensional bifurcation diagrams of the 2 variables model along *pol*, *tem*, and *exo*. **a**, **b**, **c**, equi-*tem* slices of the diagram with non-dimensional *tem* respectively equals to 1, 2, and 4. **d, e, f**, equi-*exo* slices of the bifurcation diagram with non-dimensional *exo* respectively equals to 0.15, 0.3, and 0.45. The region of stable oscillations is in gray. Yellow corresponds to the extinction region (no prey, no predators), pink to the prey-only area, and blue to the stable coexistence area.

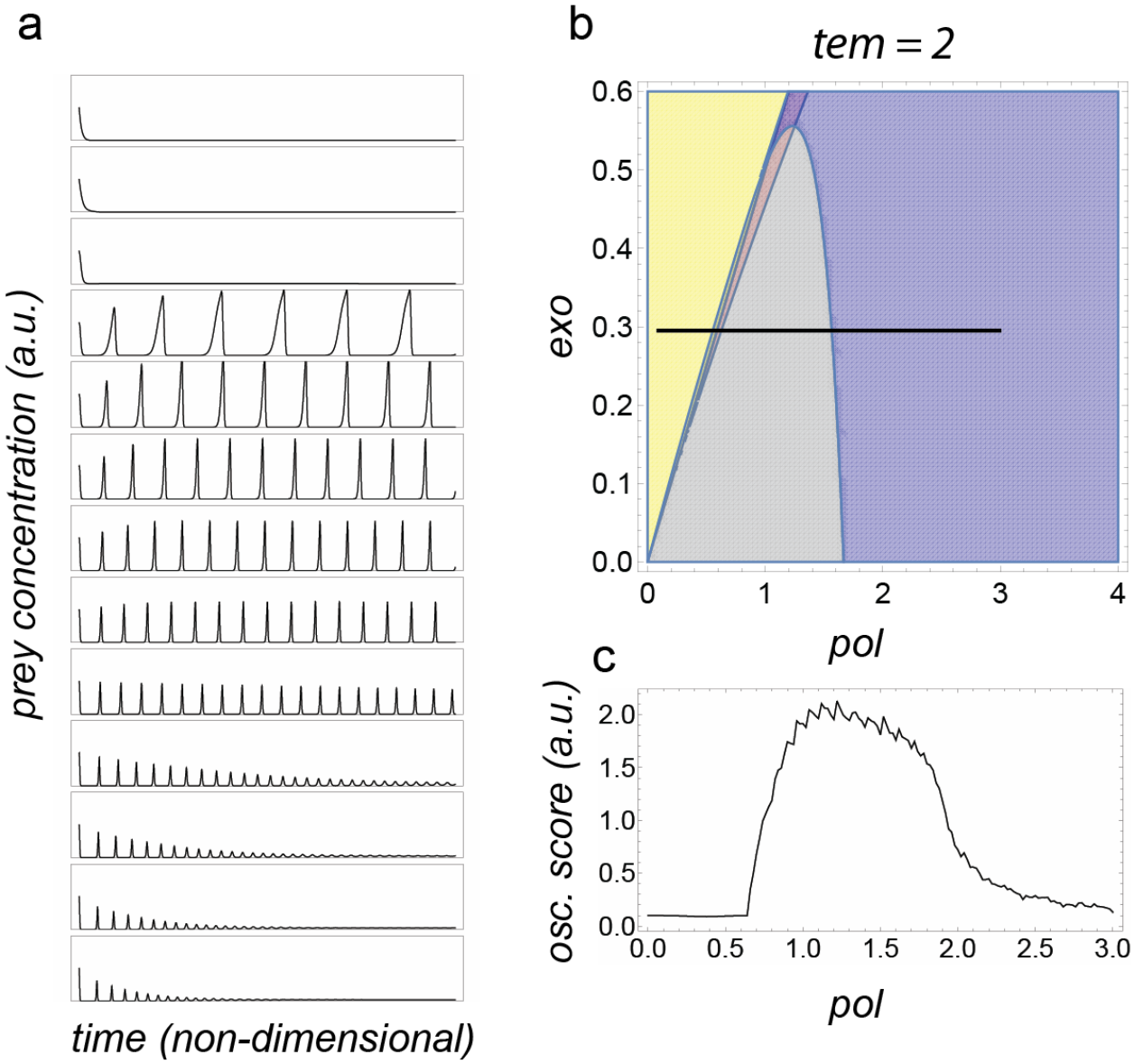

Figure S12: **a**, Numerical time traces for the two-variable model solved with the parameter set $\{tem = 2, exo = 0.3\}$ and *pol* ranging from .2 (top plot) to 3 (bottom plot) by steps of 0.2 units (corresponding to the black line in the bifurcation diagram shown in **b**. **c,** profile of computed oscillations score for the same segment in parameter space.

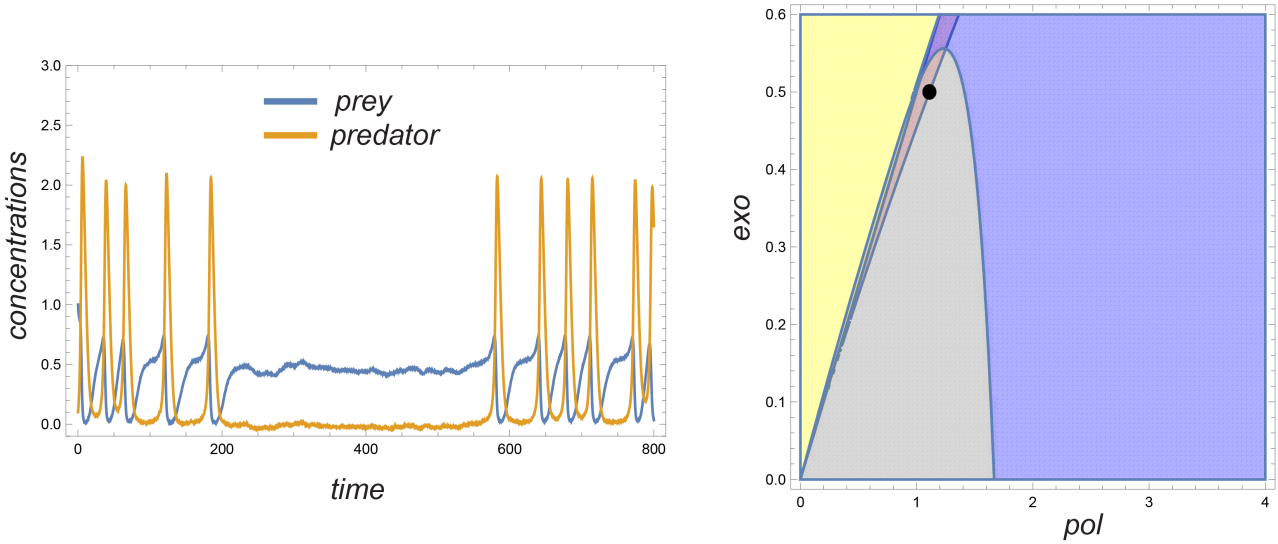

Figure S13: Stochastic bursting in the 2 variables model for oscillators close to the extinction area. Left: the ODE system with a noise component (Wiener process of amplitude 0.004, *i.e.* less than 1% of the prey concentration in the steady state) is solved for the parameter set $\{tem = 2,\ pol = 1.1,\ exo = .5\}$ represented by the black point in the bifurcation diagram shown on the right.

molecular noise in these small droplets appears to be amplified by the non linear dynamics, especially when the system is close to multiple bifurcations. The spectacular bursting of some oscillating droplets is a good example of this combination.

S9 Computational models for fits

Modeling of the bistable switch is based on the DACAD framework [22]. We model at the domain level the interactions between signal strands (short, produced and degraded endogenously) and template strands (longer, exogenous strands protected against exonuclease degradation). A given signal strand is either completely free or completely double-stranded to its complementary domain. Mismatch, partial hybridization and signal/signal or template/template interactions are ignored. The full model comprises 26 separate species interacting through 60 chemical reactions modulated by 39 parameters. Association/dissociation kinetics and enzymatic parameters are taken from [18]. Strand-displacement kinetics, dangle slowdown and stacking are derived as in [22]. The 3 models only differ by their enzymatic kinetics. For an enzyme enz acting on substrate s_i the kinetics is defined as:

$$M1: \quad \frac{V_{enz}}{K_{enz,s_i}} \cdot [s_i]$$

$$M2: \quad \frac{V_{enz}}{K_{enz,s_i} + [s_i]} \cdot [s_i]$$

$$M3: \quad \frac{V_{enz}}{K_{enz,s_i} \cdot (1 + \sum_{s_j \in substrates\ of\ enz} [s_j]/K_{enz,s_j})} \cdot [s_i]$$

with V_{enz} denoting the maximum rate for enzyme enz and K_{enz,s_i} the Michaelis constant for s_i with respect to enzyme enz. In other words, M1 is first order, M2 follows the classical Michaelis-Menten law, while M3 generalizes it by including the load of *all* substrates of an enzyme.

For each model, we iteratively optimize its parameters to fit the experimental bifurcation diagrams of the bistable switch (the target function), the set of optimized parameters depending on the model (*e.g.* M1 does not have enzymatic saturation, and thus does not optimize Michaelis parameters). We assign a fitness to a set of parameters by comparing the bifurcation diagram it predicts to the experimental diagram. Evolutionary algorithms are known

to perform particularly well in such context as they require few assumptions on the search space. We use CMA-ES [23, 24] which locally approximates the fitness gradients through stochastic sampling and evaluates the fitness sensitivity in order to avoid the pitfalls of premature convergence and flat fitness landscape. We further constrain the search to a bounded region by assigning the worst fitness to individuals whose parameters exceed specified bounds (typically 10-fold variations for enzymatic parameters and 100-fold for other parameters). Penalizing such individuals allows us to skip unnecessary ODE evaluation (which gets prohibitively slow for unrealistic parameters).

We perform 10 runs for each model, one run typically comprising 2000 evaluations (*i.e.* diagram evaluation) over 40 generations of 50 individuals. A shared set of 6 parameters (stabilization effect of stacking on all 4 templates, as well as the ratios pol/exo and nic/exo) is optimized for all models. Five additional parameters (Michaelis constants for all enzyme/substrate combinations) are optimized for M2 and M3. Optimized parameters for each model, along with their default values, are shown in Supplementary Table 3. We accelerate the evaluation of bifurcation diagrams -a major computational bottleneck- by sparsing. First, we coarse-grain the experimental diagrams of Fig. 3c (going from a ∼100×100 binning to a 20×20 binning). Secondly, we sparse these coarse diagrams by removing large and homogenous regions around the frontiers (indicated in Fig. 3f, g, h), going from 400 points to ∼200 points. Sparsing speeds up diagram computation and penalizes models that poorly approximate the positions of bifurcations. The sparse diagram is simulated for a model time of 11 hours. We then evaluate the diagram fitness as follows:

$$fit = \sqrt{\frac{\sum_{([\alpha to \alpha],[\beta to \beta]) \in conditions} dist([\alpha to \alpha],[\beta to \beta])^2}{\#conditions}}$$

with

$$\begin{aligned} dist([\alpha to \alpha],[\beta to \beta])^2 = \quad & ([\alpha toi\beta]_{l,exp,\alpha} - [\alpha toi\beta]_{l,sim,\alpha})^2 \\ & + ([\beta toi\alpha]_{l,exp,\alpha} - [\beta toi\alpha]_{l,sim,\alpha})^2 \\ & + ([\alpha toi\beta]_{l,exp,\beta} - [\alpha toi\beta]_{l,sim,\beta})^2 \\ & + ([\beta toi\alpha]_{l,exp,\beta} - [\beta toi\alpha]_{l,sim,\beta})^2 \end{aligned}$$

where $[\cdot]_l$ represents the concentration of loaded template (rescaled between 0 and 1 to match the fluorescence shift) and $\#conditions$ is the total number of points in the 2 sparsed bifurcation diagrams. We thus use the square distance between the expected concentration of loaded inhibiting template (*i.e.* those with trigger, which are contributing to most of the fluorescence) and their simulated concentrations for the given initial concentration of templates $\alpha to \alpha$ and $\beta to \beta$. Note that we sum over two different initial conditions ($\alpha\beta = 10$ and $\alpha\beta = 01$), which accounts for the four terms. The deviation of the parameters (likelihood) is computed as follows:

$$likelihood = \frac{\sum_{p \in param} |\log_{10}(\frac{current\_value_p}{initial\_value_p})|}{\#param}$$

with $param$ the set of optimized parameters for a given model. After each optimization run, we keep the best fitting solutions found at every generations (*i.e.* one candidate solution per generation). We then map them in the 2D space ($likelihood, fitness$) and draw the Pareto fronts of models, *i.e* individuals such that no other individual has simultaneously a better fitness and likelihood. Pareto fronts are commonly used in multi-objective optimization [25, 26] for identifying groups of candidate solutions that are optimal with respect to multiple criteria. A model is said to dominate another if none of the potential solution on its Pareto front are dominated by solutions from the other model. Note that a model can dominate over a particular range of parameters and be dominated over another.

All models share the same 39 parameters: initial conditions (4 signal species initial concentrations, 4 template initial concentrations, 3 enzyme concentrations), hybridization/denaturation parameters (hybridization rate, stability of all signal species, stability penalty for inhibitor on their target template compared to their generating template, left and right dangle stability increase per template, stacking denaturation slowdown for every template, invasion rate of an inhibited template by the input and output) and Michaelis-Menten parameters (activity for each enzyme, a total of five K_m). Table 3 shows which parameters where optimized for each model, along with their initial values. Details about the simulated reactions and the parameters can be found in [22]. Note that upon receiving a new enzymatic batch, we measure its activity and normalize its concentration to recover the same base activity as [18].

Enzymes Km (M2, M3)	Michaelis-Menten parameters (nM)
Km_{pol}	80
$Km_{pol,displ}$	5.5
Km_{nick}	30
$Km_{exo,signal}$	440
$Km_{exo,inhib}$	150
Stacking slowdown (M1, M2, M3)	Slowdown for the denaturation rate of input and output strands when both are present on a template separated by a nick, due to the stacking of adjacent base-pairs.
$\alpha to \alpha$	1
$\beta to \beta$	1
$\alpha toi \beta$	1
$\beta toi \alpha$	1
Enzyme concentration (M1, M2, M3)	Normalized compared to their concentrations in [18] .
Polymerase	1
Nickase	1

Table 3: Description and default values of optimized parameter. Candidate solutions always contain the parameters indicated for their model, in the order presented in this Table. Stacking slowdowns are hard to estimate or measure and left open for optimization. The impact of enzymes on the system depends partly on the relative - rather than absolute - concentrations of enzymes. As simultaneously optimizing all three concentrations may result in a correct balance between enzyme concentrations but unrealistic values, we fixed the exonuclease concentration, and evolved the concentrations of the two other enzymes.

S10 Fluorescence images and histograms of the bistable switch

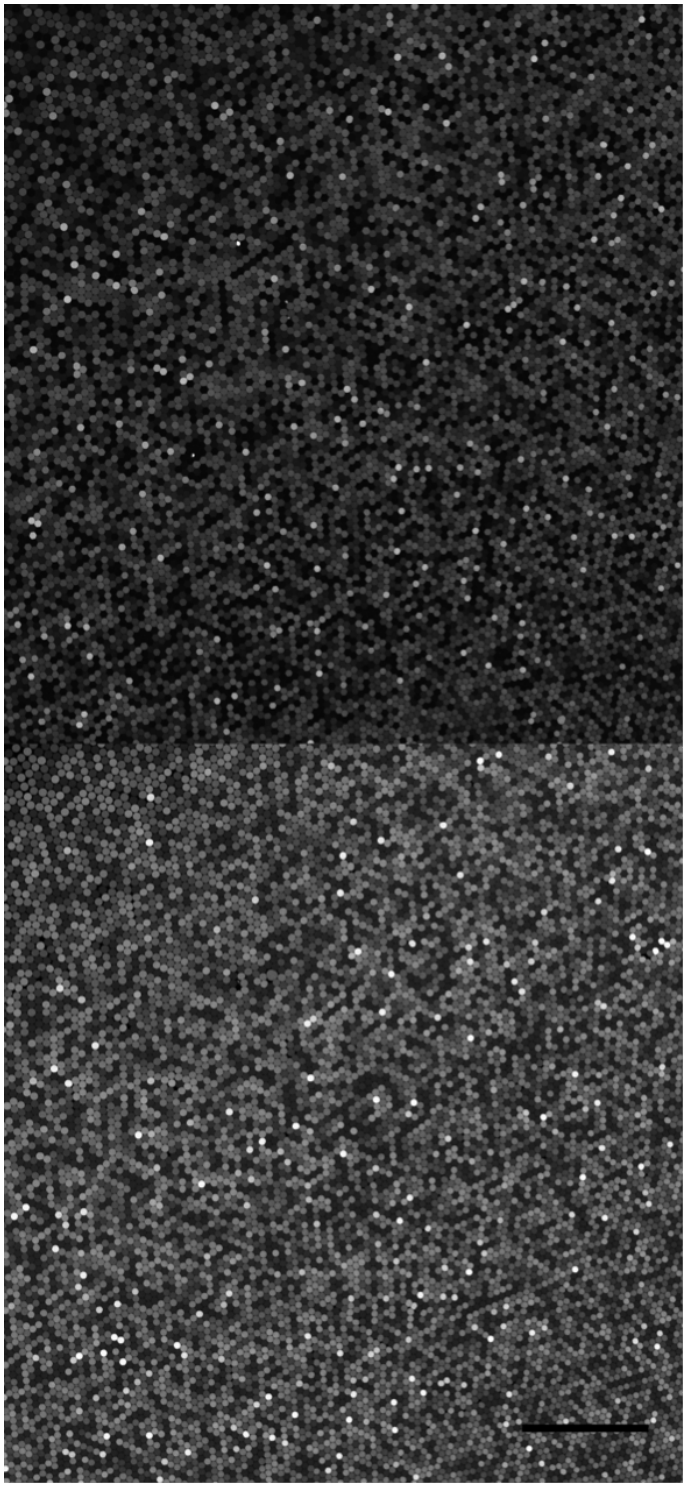

Figure S14: Fluorescence images of the barcode channels (parameter space). Top: Cascade Blue, coding for βtoβ. Bottom: Alexa647, coding for αtoα. These images correspond to the droplets generated for experiment of Fig. 3c (bistable circuit started in αβ =01). The scale bar is 1 mm. The image contains about 10 000 droplets. Their diameter is 62 µm (+/- 10%). The brightest droplets correspond to the apex of the calibration arms.

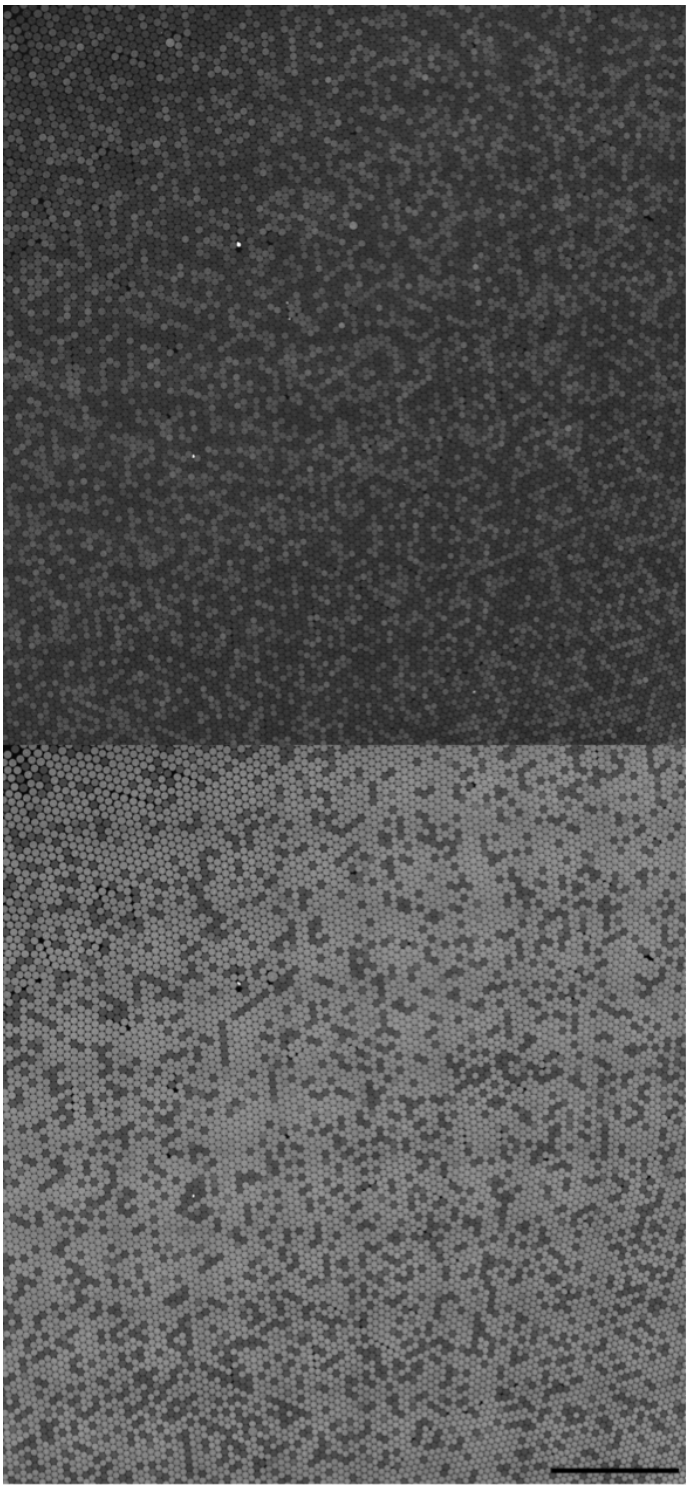

Figure S15: Fluorescence images of the channels for the dynamic observables. Top FAM, reporting the presence of α (dim droplets). Bottom: TAMRA, reporting the presence of β (bright droplets). The scale bar is 1 mm. To avoid calibration issues, the dyes have been attached to the inhibitory templates and are hence present at the same concentration in all droplets (only the concentration of the autocatalytic templates change during the microfluidic scanning). Therefore, the level of α or β in a given droplet can be inferred from the raw intensity in the corresponding reporting channel.

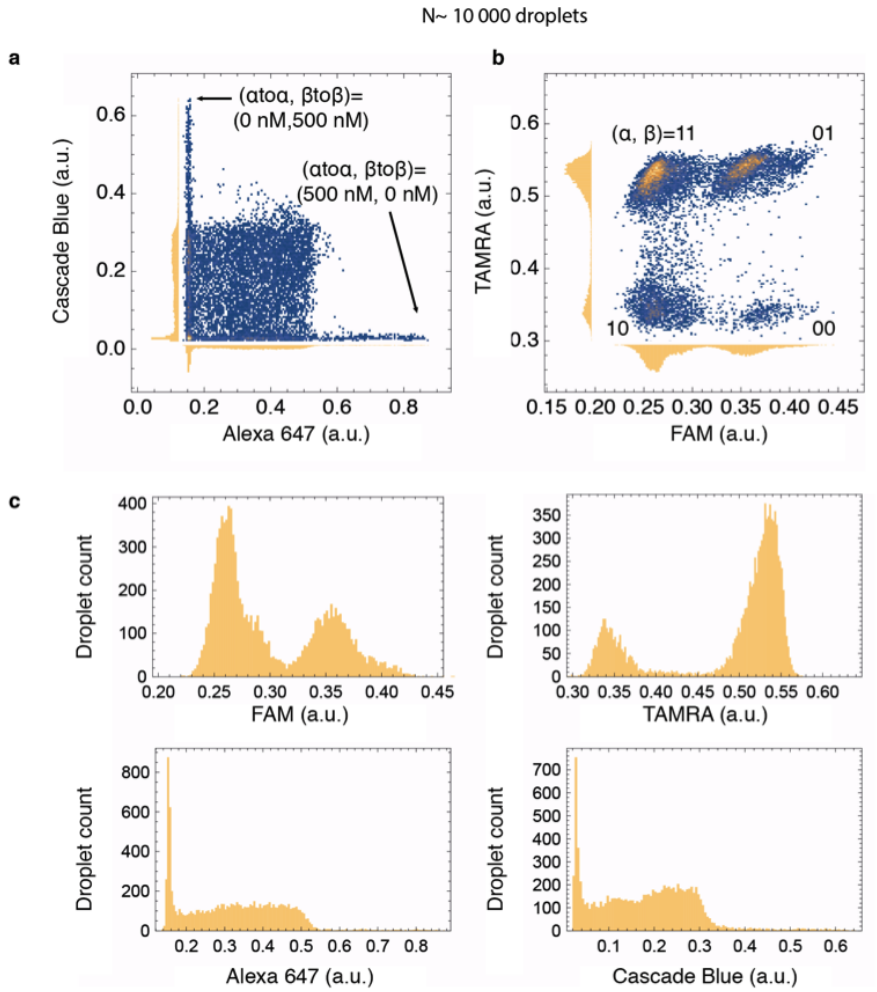

Figure S16: Distribution of raw fluorescence in droplets. **a**, Coverage of the parameters space. The density histogram shows the fluorescence of droplets in the (Alexa647, Cascade Blue) space. In addition to the square plotted in Fig. 3c, the microfluidic pressure script also explores vertical and horizontal arms along the axis. Their apexes serve for calibration, indicating the fluorescence of droplets with a maximal amount of template αtoα or βtoβ. **b**, Density histogram of (FAM, TAMRA), which are proxies of (α, β). Low levels of α translate into high levels of FAM, while high levels of TAMRA translate to high levels of β. The histogram of the projected distribution is shown on the side. **c**, 1D histograms of the individual fluorescence channels.

S11 Droplet array and time traces for the predator-prey system

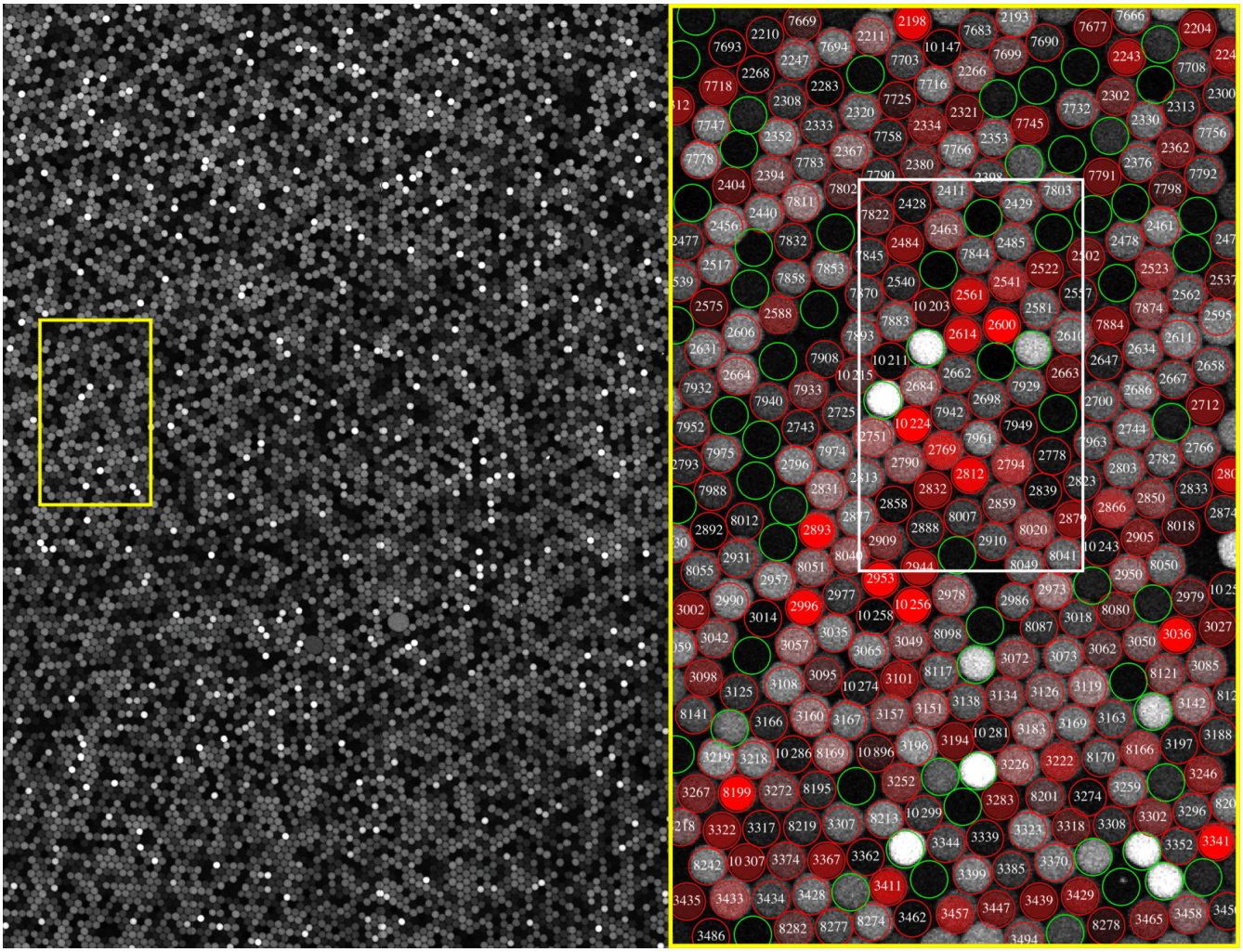

Figure S17: Droplet array for the predator-prey system. Left: The first (out of 798) image in the observation (TAMRA) channel. Right: zoom on the inset. 368 droplets were detected in this image. 65 of them (circled in green) belong to the self-calibration axes, *i.e.* they have a quasi-null value in two of the three fluorescent barcodes. These are used only during the conversion of barcodes intensities into absolute concentration units, and then dropped for the rest of the analysis. The remaining 245 droplets, circled in red, are used for building the bifurcation diagram. The intensity of the red shading for these droplets is proportional to their oscillation score. The number (in white) is attributed during droplet tracking and is kept as a unique identifier during further processing (see Fig. S18). The white rectangle shows the area plotted in Fig. 4b of the main text.

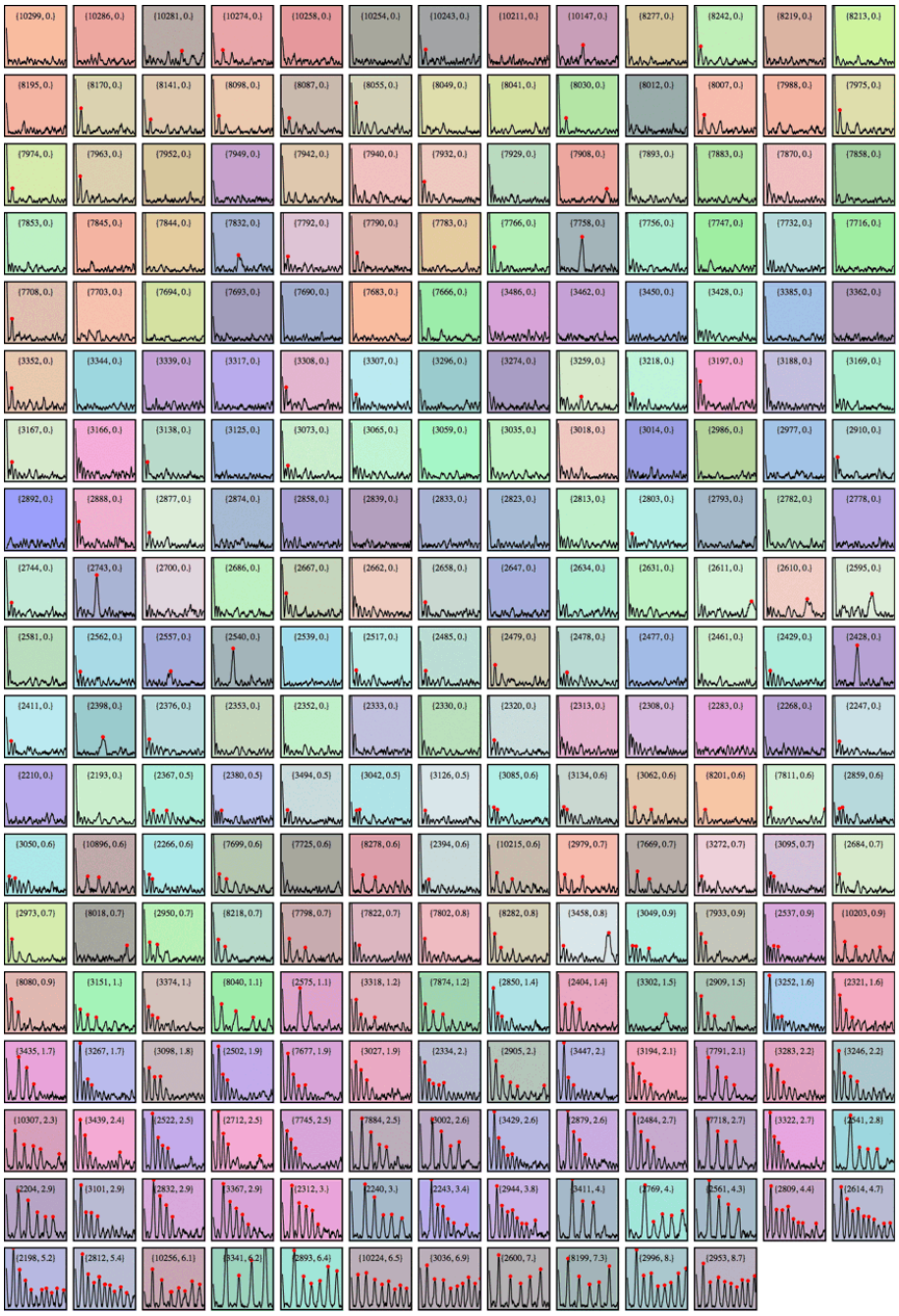

Figure S18: 245 time traces extracted from the area shown in Fig. S17. The plots show the temporal evolution of the fluorescence of droplets (spatially integrated over the whole droplet and after detrending) over 25 hours. Time traces that showed parasitic side reactions (N=58), as well as droplets not belonging to the cube (N=65 droplets marked green in Fig. S17), were filtered out. The x-axis indicates time (from 0 to 25 hours) and the y-axis the fluorescence level (arbitrary but identical unit for all traces). The inset shows the droplet identifier, together with the oscillation score. The background color is the RGB combination of the normalized barcodes (*i.e.* red content = [polymerase]/26; green content = [template]/380; blue content = [exonuclease]/115)

S12 Parasitic reactions

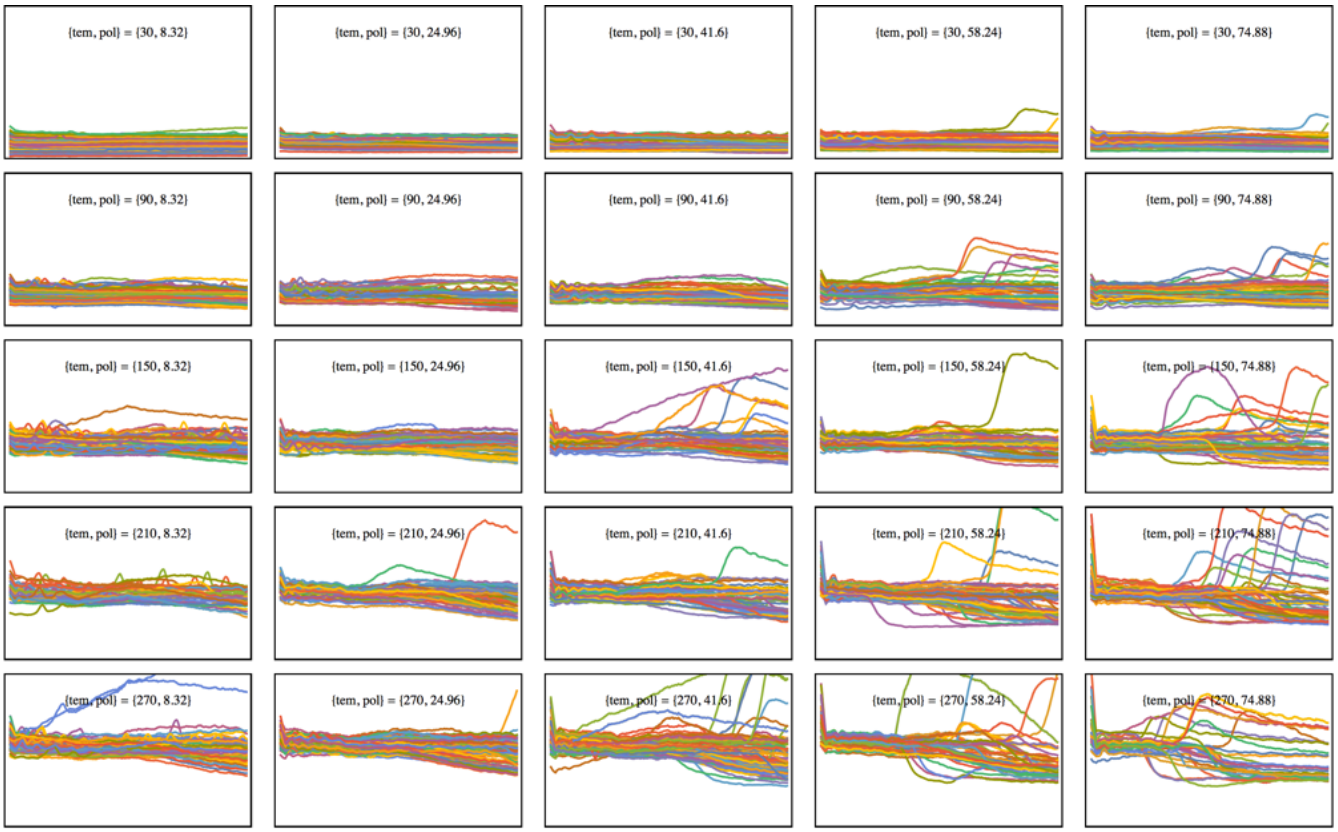

Figure S19: Parasitic reactions tend to overtake the system at long times, especially for high pol and/or high template concentrations. This figure shows a total of 2000 randomly selected raw time-traces, classified by template (in nM) and polymerase concentration (in U/ml) (*i.e.* the plots in each box are not replicates and can have very different levels of exonuclease). The x-axis is the time, running from 0 to 40 hours. The y-axis is the fluorescence level in the TAMRA channel, with the same arbitrary unit for all plots. The stochastic appearance of parasites in droplets can be detected because it induces a strong positive or negative shift in the florescence intensity. This shift is generally much stronger that the one induced by normal prey-amplification reaction during oscillations or convergence to a steady state. Traces colors are arbitrary.

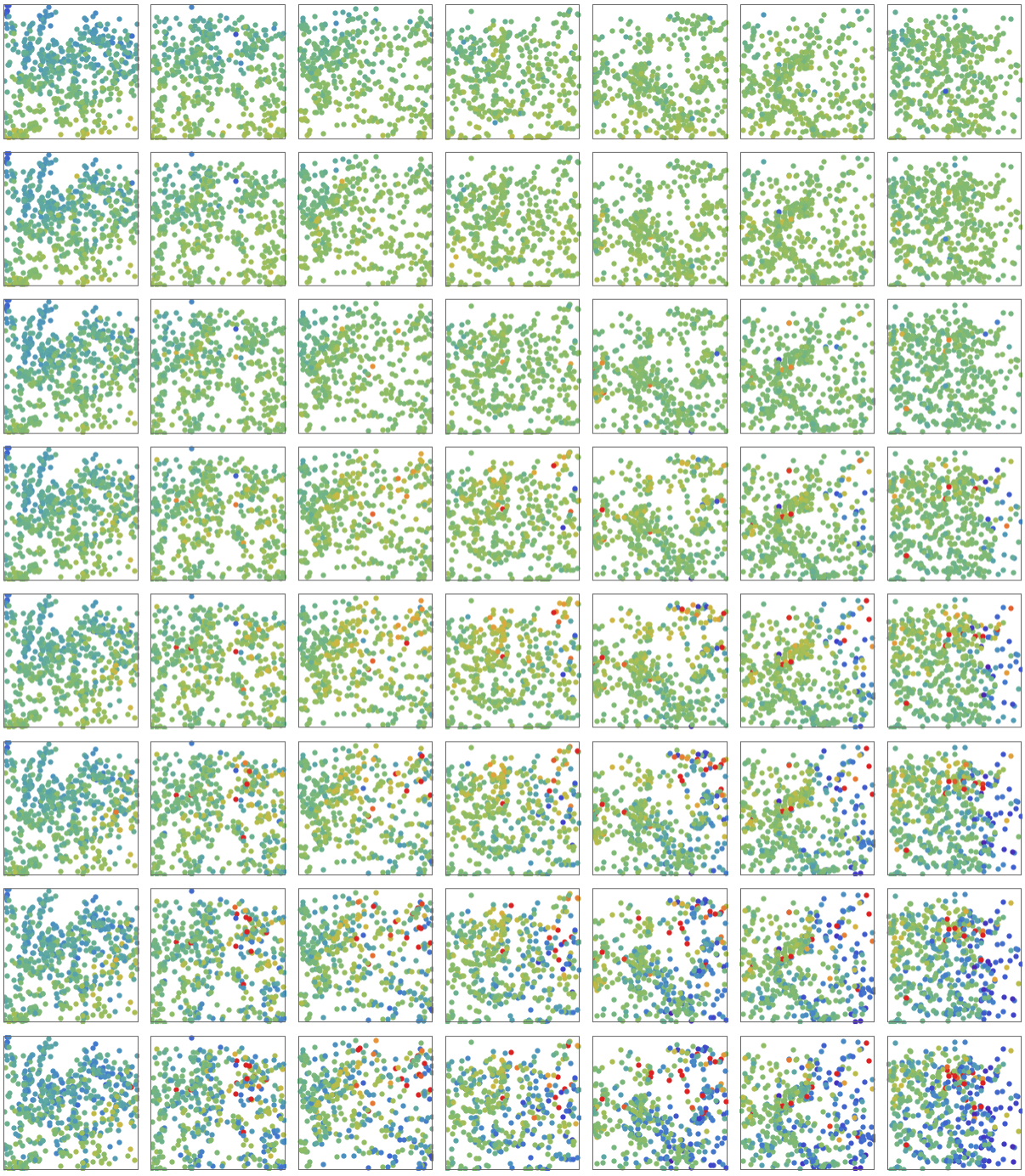

Figure S20: Parasitic reactions appear stochastically in some - but not all - droplets. Each row contains 7 cuts along the template axis *i.e*, all droplets contained in a slice centered at respectively (from left to right) 40, 80, 120, 160, 200, 240, 280 nM of template, and arranged in the plane pol (x-axis, running from 0 to 26 U/mL) / exo (y-axis, running from 0 to 115 nM). Time is going from 1 hour (top row) then 6, 11, 16, 21, 26, 31, 36 hours (bottom row). The color codes for fluorescence intensity in the TAM channel, normalized to the local average. In this representation, droplets whose fluorescence shows a strong shift (indicating a parasitic reaction) appear in blue (negative shift) or red (positive shift) on the rainbow color scale.

S13 Typical concentrations ranges of predators and preys

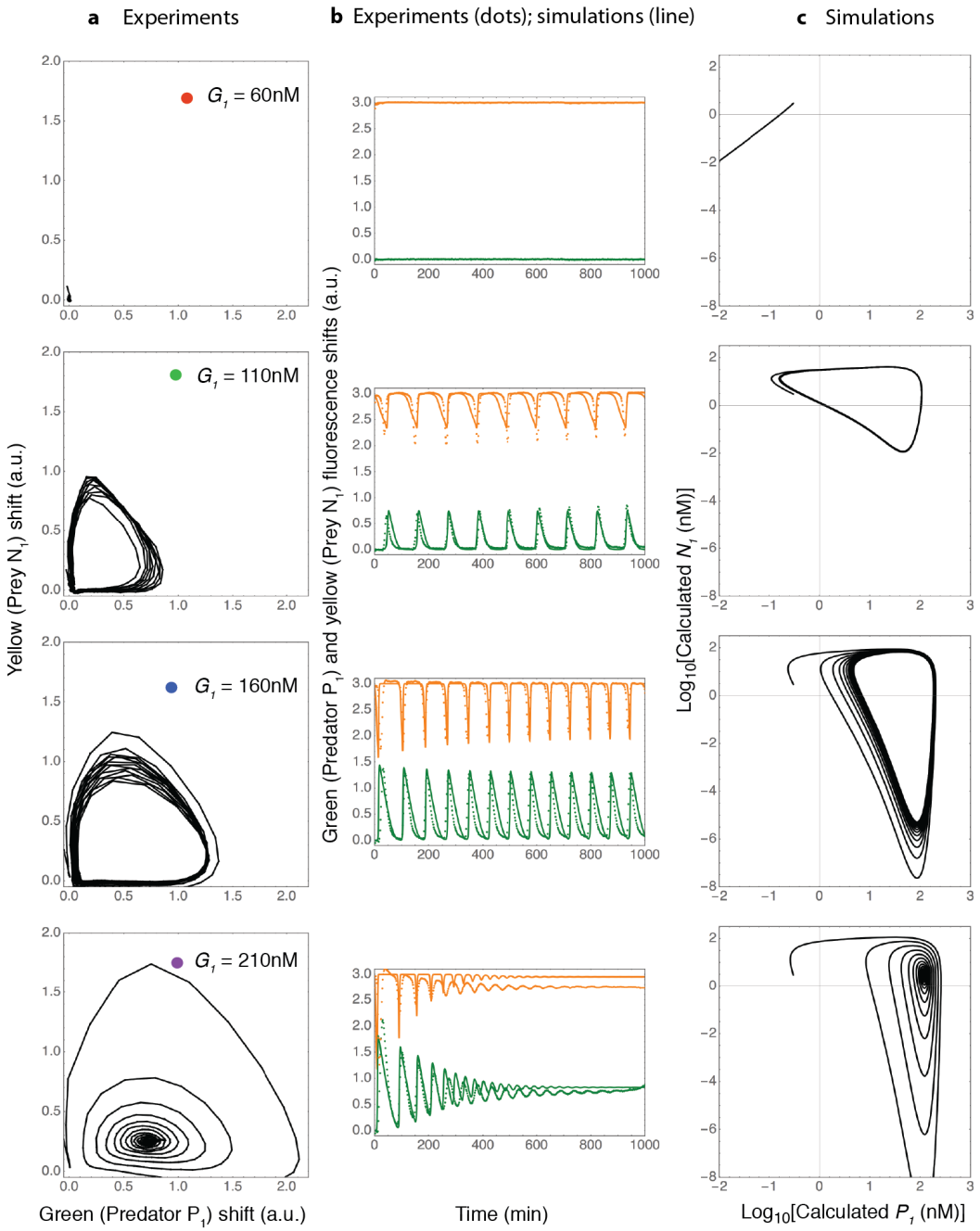

Figure S21: **Typical dynamics and concentrations ranges for predators and preys**. The figure is adapted from Figure 3 from [20] and shows experimental and fitted time plots for various template concentrations in test tube experiments. The only difference with the original figure is the logarithmic axes in c. Dots are experimental data and the continuous lines are the model prediction, using the same set of optimized parameters for all four experiments. **a** Fluorescent records of the experimental 2D trajectories. **b** time traces. **c** the simulated trajectory (same as in b) in concentration space shows the low concentration of prey that is reached for some experimental conditions at the minimum of the cycle.

References

[1] A. Padirac, T. Fujii, and Y. Rondelez. Quencher-free multiplexed monitoring of dna reaction circuits. *Nucleic Acids Research*, 40(15):e118, 2012.

[2] C. Holtze, A. C. Rowat, J. J. Agresti, J. B. Hutchison, F. E. Angile, C. H. J. Schmitz, S. Koster, H. Duan, K. J. Humphry, R. A. Scanga, J. S. Johnson, D. Pisignano, and D. A. Weitz. Biocompatible surfactants for water-in-fluorocarbon emulsions. *Lab on a Chip*, 8(10):1632–1639, 2008.

[3] D. C. Duffy, J. C. McDonald, O. J. A. Schueller, and G. M. Whitesides. Rapid prototyping of microfluidic systems in poly(dimethylsiloxane). *Analytical Chemistry*, 70(23):4974–4984, 1998.

[4] S. Kaneda, K. Ono, T. Fukuba, T. Nojima, T. Yamamoto, and T. Fujii. Modification of the glass surface property in pdms-glass hybrid microfluidic devices. *Analytical Sciences*, 28(1):39–44, 2012.

[5] Jean-Christophe Baret, Felix Kleinschmidt, Abdeslam El Harrak, and Andrew D. Griffiths. Kinetic aspects of emulsion stabilization by surfactants: A microfluidic analysis. *Langmuir*, 25(11):6088–6093, 2009.

[6] J. C. Lotters, W. Olthuis, P. H. Veltink, and P. Bergveld. The mechanical properties of the rubber elastic polymer polydimethylsiloxane for sensor applications. *Journal of Micromechanics and Microengineering*, 7(3):145–147, 1997.

[7] Arthur D Edelstein, Mark A Tsuchida, Nenad Amodaj, Henry Pinkard, Ronald D Vale, and Nico Stuurman. Advanced methods of microscope control using micro-manager software. *Journal of Biological Methods*, 1(2):e11, 2014.

[8] K. Hasatani, M. Leocmach, A. J. Genot, A. Estevez-Torres, T. Fujii, and Y. Rondelez. High-throughput and long-term observation of compartmentalized biochemical oscillators. *Chemical Communications*, 49(73):8090–8092, 2013.

[9] Buitelaar R.M., Bucke C., Tramper J., and Wijffels R.H., editors. *Immobilized Cells: Basics and Applications: Basics and Applications*, page 202. Elsevier, 2006.

[10] G. L. Lukacs, P. Haggie, O. Seksek, D. Lechardeur, N. Freedman, and A. S. Verkman. Size-dependent dna mobility in cytoplasm and nucleus. *Journal of Biological Chemistry*, 275(3):1625–1629, 2000.

[11] Y. P. Bai, X. M. He, D. S. Liu, S. N. Patil, D. Bratton, A. Huebner, F. Hollfelder, C. Abell, and W. T. S. Huck. A double droplet trap system for studying mass transport across a droplet-droplet interface. *Lab on a Chip*, 10(10):1281–1285, 2010.

[12] Maximilian Weitz, Jongmin Kim, Korbinian Kapsner, Erik Winfree, Elisa Franco, and Friedrich C. Simmel. Diversity in the dynamical behaviour of a compartmentalized programmable biochemical oscillator. *Nature Chemistry*, 6(4):295–302, 2014.

[13] D. Pekin, Y. Skhiri, J. C. Baret, D. Le Corre, L. Mazutis, C. Ben Salem, F. Millot, A. El Harrak, J. B. Hutchison, J. W. Larson, D. R. Link, P. Laurent-Puig, A. D. Griffiths, and V. Taly. Quantitative and sensitive detection of rare mutations using droplet-based microfluidics. *Lab on a Chip*, 11(13):2156–2166, 2011.

[14] Jung-uk Shim, Rohan T. Ranasinghe, Clive A. Smith, Shehu M. Ibrahim, Florian Hollfelder, Wilhelm T. S. Huck, David Klenerman, and Chris Abell. Ultrarapid generation of femtoliter microfluidic droplets for single-molecule-counting immunoassays. *Acs Nano*, 7(7):5955–5964, 2013.

[15] J. C. Baret, O. J. Miller, V. Taly, M. Ryckelynck, A. El-Harrak, L. Frenz, C. Rick, M. L. Samuels, J. B. Hutchison, J. J. Agresti, D. R. Link, D. A. Weitz, and A. D. Griffiths. Fluorescence-activated droplet sorting (fads): efficient microfluidic cell sorting based on enzymatic activity. *Lab on a Chip*, 9(13):1850–1858, 2009.

[16] Siavash Kijani, Ulf Yrlid, Maria Heyden, Malin Levin, Jan Boren, and Per Fogelstrand. Filter-dense multicolor microscopy. *Plos One*, 10(3), 2015.

[17] J. N. Zadeh, C. D. Steenberg, J. S. Bois, B. R. Wolfe, M. B. Pierce, A. R. Khan, R. M. Dirks, and N. A. Pierce. Nupack: Analysis and design of nucleic acid systems. *Journal of Computational Chemistry*, 32(1):170–173, 2011.

[18] A. Padirac, T. Fujii, and Y. Rondelez. Bottom-up construction of in vitro switchable memories. *Proceedings of the National Academy of Sciences of the United States of America*, 109(47):E3212–E3220, 2012.

[19] Lei Dai, Daan Vorselen, Kirill S. Korolev, and Jeff Gore. Generic indicators for loss of resilience before a tipping point leading to population collapse. *Science*, 336(6085):1175–1177, 2012.

[20] T. Fujii and Y. Rondelez. Predator-prey molecular ecosystems. *Acs Nano*, 7(1):27–34, 2013.

[21] J.D Murray. *Mathematical Biology*, volume 17 of *Interdisciplinary Applied Mathematics*. Springer, third edition, 2004.

[22] Nathanael Aubert, Clement Mosca, Teruo Fujii, Masami Hagiya, and Yannick Rondelez. Computer-assisted design for scaling up systems based on dna reaction networks. *Journal of the Royal Society Interface*, 11(93), 2014.

[23] N. Hansen, S. D. Muller, and P. Koumoutsakos. Reducing the time complexity of the derandomized evolution strategy with covariance matrix adaptation (cma-es). *Evolutionary Computation*, 11(1):1–18, 2003.

[24] N. Hansen and A. Ostermeier. Completely derandomized self-adaptation in evolution strategies. *Evolutionary Computation*, 9(2):159–195, 2001.

[25] R. T. Marler and J. S. Arora. Survey of multi-objective optimization methods for engineering. *Structural and Multidisciplinary Optimization*, 26(6):369–395, 2004.

[26] A. E. Eiben and James E. Smith. *Introduction to Evolutionary Computing.* Natural Computing Series. Springer, 2015.